Note: Preprint Version. Please Cite: Desai, S., Schetz, J. A., Kapania, R. K., & Gupta, R. (2024). Wind Tunnel Testing of Tethered Inflatable Wings. Journal of Aircraft, 1-18. https://arc.aiaa.org/doi/10.2514/1.C037437

Wind Tunnel Testing of Tethered Inflatable Wings

Siddhant Desai *, Joseph A. Schetz †, and Rakesh K. Kapania‡
Virginia Tech, Blacksburg, VA 24060

Rikin Gupta §
Toyota Research Institute North America, Ann Arbor, MI 48105

A wind tunnel testing approach for tethered inflatable wings is presented*. Use cases for such wings range from airborne wind energy systems to high-altitude communication platforms. The tests were conducted for two tethered inflatable wings, one made out of nylon fabric and the other an ultra-high-molecular-weight polyethylene fabric. They were tested within a speed range of 15 to 32.5 m/s for three tether attachment configurations. Stereo photogrammetry data, force and moment measurements, and wake pressure measurements were recorded for each speed and test configuration. These measurements provide an experimental database for aeroelastic model validation and comparisons with high-fidelity computational fluid dynamics studies. The effects of wing fabric material and tether attachment configurations on aerodynamic performance were explored and found to have a profound impact. These tests also highlight the possibility of passive aeroelastic tailoring of the wing configuration to achieve desired aerodynamic performance in the form of high lift and load alleviation. Some testing challenges and possible sources of measurement uncertainty are also discussed.

Nomenclature

Variables:

AR	=	Aspect Ratio
b	=	span length, m
$\bar{b}$	=	reference span length, m
C_p	=	pressure coefficient
c	=	chord length, m
α	=	angle of attack

*Graduate Research Assistant, Kevin T. Crofton Department of Aerospace and Ocean Engineering, AIAA Member, Presently Application Engineer II, Ansys Inc., spdesai@vt.edu

†Fred D. Durham Endowed Chair Emeritus, Kevin T. Crofton Department of Aerospace and Ocean Engineering, AIAA Life Fellow

‡Mitchell Professor, Kevin T. Crofton Department of Aerospace and Ocean Engineering, AIAA Fellow

§Research Engineer, Future Mobility Research Department, AIAA Member, Presently Sr. Loads and Dynamics Engineer, Supernal, rg1993@vt.edu

*Preliminary results were previously presented as conference article AIAA 2022-0903 at the AIAA SciTech 2022 Forum in San Diego, CA, held between January 3-7, 2022.

F = force, N

M = moment, N·m

T = tether tension, N

t = airfoil maximum thickness, m

θ_e = elastic twist angle, deg

θ_r = pretest rigid twist angle, deg

P = pressure, Pa

ρ = air density, kg/m^3

σ = standard deviation

δ = wind tunnel static deformations, m

R = radial distance for RBF interpolation, m

Re = Reynolds number

U = velocity, m/s

y = distance along the span, m

X, Y, Z = reference coordinate axes for experimental measurements

Subscripts:

$(\cdot)_\infty$ = ambient/freestream value

$(\cdot)_0$ = total/stagnation value

$(\cdot)_{LE}$ = leading edge quantity

$(\cdot)_{TE}$ = trailing edge quantity

I. Introduction

Tethered kites have historically had a large variety of applications ranging from weather monitoring research to military-related applications[1]. A seminal article on crosswind kite power by Loyd [2] resulted in research efforts directed towards studying the use of tethered kites for AWE generation [3–6]. As a consequence, a High-Altitude Aerial Platform (HAAP) project comprising a large-scale, tethered, inflatable, flying wing kite, the applications of which are envisioned to include atmospheric data acquisition, airborne communication relay, Airborne Wind Energy (AWE) generation, transportation, and disaster relief [7, 8] was undertaken. As part of this project, feasibility studies for an AWE system utilizing a tethered kite were conducted by Nam et al. [8]. Subsequent efforts included the development and testing of flight dynamics models and control systems for this application [9–11].

Hobbs [1] laments the limited number of formalized studies of the kite system and its aerodynamics. Rogallo [12] acknowledges the challenges related to testing such flexible wings due to their inherent coupling of the aerodynamic

performance to the structural response and the uncertainties involved in testing such a system. Most kites tend to have wings built out of fabric, supported by spars and struts along their spans. Some designs instead utilize inflated tubular spars to rigidize the wing structure, while some rely on ram-air inflation. In the past, wind tunnel tests have been conducted for ram-air inflated wings due to their use in paragliders, parafoils, airborne wind energy (AWE) applications, launch vehicle part recovery, etc. [13]. The ram-air inflated wing shape relies heavily on the free-stream dynamic pressure and angle of attack. Hence, aerodynamic testing usually involves a representative rigid or semi-rigid wind tunnel model [14, 15]. These flexible ram-air inflated wings possess a limitation of collapse under low free-stream dynamic pressure. Sealed and pressurized inflated wings do not exhibit such a limitation, but very few wind tunnel tests have been conducted to study and characterize their aerodynamic performance [16–18].

Such inflatable wings are cost-effective to build, durable, and lightweight [19–21]. This makes them ideal for tethered kites where weight savings are critical. Norris and Pulliam [22] provide a detailed review of the historical development of such inflatable wings for various aircraft. These use cases include aircraft such as the Goodyear Inflatoplane, the Apteron UAV, the I2000 NASA research aircraft, and several aircraft forming part of the BIG BLUE project [21–25]. Brown et al. [20] and Cadogan et al. [23] discuss various construction methods for inflatable wings. Recent designs involve multi-cellular, baffled, inflatable structures resembling a series of intersecting cylinders. They can provide the requisite rigidity to the wing at lower inflation pressures than previous designs [22, 26]. The internal bladder material is usually polyurethane or similar, while the restraint material is a high-strength fabric like Vectran, Kevlar, etc. Whether these tubes are arranged spanwise or chordwise, they result in wing surface undulations on inflation.

This paper focuses on pressure-sealed inflatable wings with chordwise surface undulations, which provide greater spanwise rigidity. The aerodynamics over such wing sections have previously been studied experimentally and numerically [27–29]. These studies find that chordwise undulations on the airfoil section results in an increase in drag and reduction in the lift when compared with classical airfoil sections [23, 24]. A lot of the studies involving such airfoil sections are directed at low Reynolds number applications, with some evidence suggesting that better aerodynamic performance is achievable with these “bumpy" shaped profiles at low chord Reynolds numbers ($\sim$100k) and high angles of attack (greater than $\sim$10 degrees), when compared with a smooth airfoil counterpart [24, 30, 31]. These studies remain largely inconclusive, and the drag penalty due to these chord-wise undulations at lower angles of attack complicates the matter. As a result, it has become imperative to cover the wing with lightweight skin to maintain a smooth aerodynamic shape with predictable aerodynamic performance over the operating range of the design.

Previous experiments [16–18] for such wings have studied the effect of angle of attack on either aeroelastic deformation or lift coefficient for a fixed/limited set of dynamics pressures for untethered inflatable wings. These experiments either measure aeroelastic deformations or forces and moments but none simultaneously measure both. A comparison of the test articles for these experiments, and their testing configurations, have been tabulated in Table 1, along with that of the present inflatable wing wind tunnel test conducted at Virginia Tech. The test by Okda et al. [16]

attempts to obtain the two-dimensional lift and drag coefficients of an inflatable airfoil section. Due to wing flexibility, this approach may not be suitable as the flow is likely to be three-dimensional. Furthermore, no wing displacement data were collected during these tests, which may hinder in obtaining more detailed inferences. The wind tunnel test by Simpson et al. [17] measures this displacement field over a cambered finite AR inflatable wing for a range of wind tunnel dynamic pressures, angles of attack, and internal inflation pressures, using a 3D photogrammetry system.

As part of the current study, the angle of attack is kept fixed as the focus is to study the effect of wing fabric and tether attachment configurations as described later on. Another reason for fixing the angle of attack is that pre-test predictions using an in-house computational model [32] showed that higher angles of attack would lead to the loads on the wing exceeding the limits of the measurement instrumentation (both the 6-axis load cells and the tension measurement load cells) due to the non-linear increase in forces and moments. This choice is also supported/vindicated by the force and moment data shown in Section III.B. Finally, altering the angle of attack requires varying the boundary conditions for the tethers which will alter the way the wings deform. On the other hand, the inflation pressure is limited to 2.5 psi due to constraints on the capacity of the wing to hold high inflation pressures while maintaining acceptable leak rates to allow for continuous testing. To the author's knowledge, no previous test monitors and records simultaneously the displacement field and aerodynamic forces and moments for such a tethered inflatable wing.

Table 1 Comparison of Various Wind Tunnel Tests of Inflatable Wings

	Okda et al. [16]	Cocke [18]	Simpson et al. [17]	Current Study
Wind Tunnel	Chalmers Low Speed Tunnel	Langley Full-Scale Tunnel	Eiffel Type Low Speed Tunnel	VT Stability Wind Tunnel
Wind Tunnel Cross-Section	1.25 m × 1.80 m (4.1 ft. × 6 ft.)	9.14 m × 18.28 m (30 ft. × 60 ft.)	0.61 m × 0.61 m (2 ft. × 2 ft.)	1.85 m × 1.85 m (6 ft. × 6 ft.)
Wind Tunnel Turbulence	∼ 0.15%	0.14% – 1.05%	∼ 0.25%	0.016% – 0.033%
Model Geometry	b = 1.00 m c = 1.00 m AR = 1.0	b = 6.70 m c = 1.52 m AR = 4.4	b = 0.45 m c = 0.33 m AR = 1.36	b = 1.17 m c = 0.31 m AR = 3.8
Base Airfoil	NACA 0021	NACA 0015	NACA 4318	NACA 0015
Test Article Configuration	Straight Rectangular	Complete Aircraft	Straight Rectangular	30° Swept Rectangular
Tethers/Cables	No	With Guy Cables	No	LE and TE Tethers
Inflation Pressure, kPa (psig)	50 (7.3), 100 (14.5), 150 (21.7)	20.7 (3)–48.3 (7)	13.8 (2), 27.5 (4), 41.4 (6)	13.79 (2.5)
Test Velocity, m/s	10	16.1 – 31.7	12.8 – 25.6	15 – 32.5
Angle of Attack	−20° to +20°	−12° to +8°	−4° to +16°	2.5°
Re_c	651k	1136 – 1941k	300 – 600k	268 – 634k

In preparation for the current wind tunnel tests, static and vibration tests were also conducted for validation and

fine-tuning of a structural model of these inflatable wings [33, 34]. For accurate estimation of aeroelastic effects, a more detailed understanding of inflatable wing aerodynamics is imperative. Furthermore, the aerodynamic performance of such flexible wings cannot be decoupled from the effects of in-flight structural deformation since these deformations are large enough to impact the flow over the wing. The primary research goal of this work involves creating a comprehensive database for aeroelastic and CFD model validation. Additionally, the aerodynamic performance of flexible inflatable wings is studied using two inflatable wing test articles, one constructed from nylon fabric and the other from an Ultra-High-Molecular-Weight Poly-Ethylene (UHMWPE) fabric. Three different tether attachment configurations were tested, and the effects of the configuration and fabric material on the aerodynamic performance of these flexible inflated wings are discussed. The following sections discuss the experimental setup and methodology, followed by static aeroelastic displacement field results, forces and moments, and wake pressures, and finally, conclusions and future work.

II. Experimental Setup and Methodology

A. Overview of Wind Tunnel Test Facility

The Virginia Tech Stability Wind Tunnel is one of the largest university-owned wind tunnels in the United States [35]. The facility is a closed-circuit, subsonic wind tunnel with a test section that is 7.32 m long and has a 1.85 m $\times$ 1.85 m square cross-section. Due to the presence of seven turbulence screens, the turbulence intensity within the tunnel is very low, ranging from 0.016% at 12 m/s to 0.031% at 57 m/s [36], and the maximum operating speed of the tunnel is 80 m/s (in the absence of blockage). This allows for conducting wind tunnel tests up to a Reynolds number of 5×10^6/m. Flow through the tunnel is driven by a custom-built 4.3 m diameter fan powered by a 0.45 MW variable speed DC motor with a maximum angular velocity of 600 RPM. Although the wind tunnel is a closed-circuit type, it does include an air exchange tower open to the atmosphere, which allows for some temperature stabilization within the test section [35].

Downstream of the air exchange tower lies a 5.5 m $\times$ 5.5 m cross-section settling chamber, which then directs the flow into the test section via a 9:1 contraction nozzle. Recently, aluminum modular wall inserts and a new contraction liner were designed for the anechoic test section of the wind tunnel [36, 37]. These aluminum wall inserts provide the capability to build custom aluminum paneling for the test section side walls for ease of instrumentation access. To supplement the anechoic test section for aeroacoustic testing, two acoustically treated anechoic chambers were installed behind both the port and starboard side walls of the test section. They are 6.0 m $\times$ 4.2 m $\times$ 2.8 m in dimension and allow for additional reduction of acoustic reflections while also providing a place for housing test instrumentation. For the inflatable wing tests, the anechoic test section with the modular aluminum wall inserts was employed. The anechoic chamber behind the test section port-side wall was cleared for placing some of the test instrumentation, including the computers, data acquisition systems, and the 3D photogrammetry setup.

B. Test Article Construction and Design

The first inflatable wing was built using Nylon 200D fabric with a cross-section consisting of 8 baffles (webs) connecting the top and bottom skins. The top and bottom skins are bonded to the baffles with an impulse heating technique, and the peel strength in force per unit length of these connections is found to be 0.8 N/mm [33]. The chord length of the wing pre-inflation is 0.35 m, and the span is 1.3 m [33]; however, these are not the reference span and chord lengths, since only about 1.17 m of the wing are exposed to the air, while an aluminum mount shrouds the rest. The design of this mount, as well as the decision to sweep the wing and mount, are discussed later in this section. The second inflatable wing was built in an identical fashion using an UHMWPE fabric. The chosen fabric material for this wing is the Dyneema® composite fabric (CT5K.18/W23) [38], which is found to be significantly stiffer than the Nylon 200D fabric. These wings are illustrated in Fig. 1.

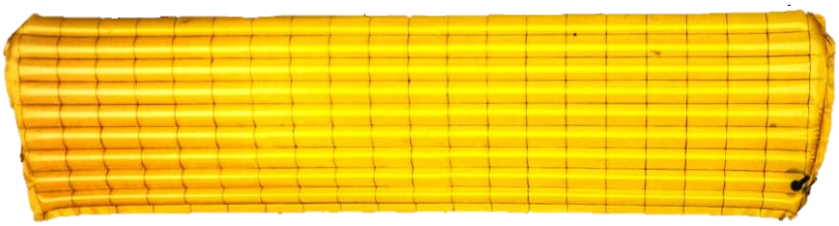

(a) Nylon 200D Inflatable Wing Test Article

(b) UHMWPE Inflatable Wing Test Article

Fig. 1 (a) Nylon 200D Inflatable Wing Test Article with an Inflation Valve on the Lower Right, and (b) UHMWPE Inflatable Wing Test Article

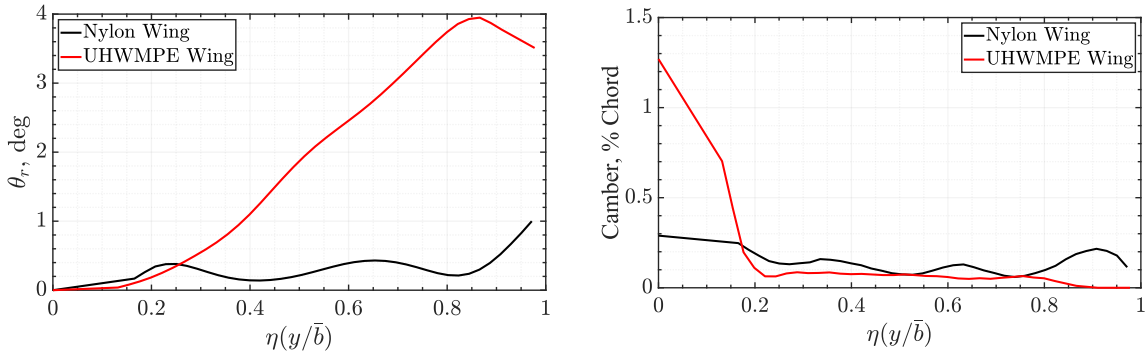

(a) Twist **(b) Camber**

Fig. 2 Pretest Inflated Rigid Wing Spanwise Geometry Distribution

Both wings are designed to follow the standard NACA 0015 airfoil profile [39], albeit with surface undulations, resulting in an increased t/c of 20% on inflation when compared to the design t/c of 15%. Interestingly, even though the UHMWPE wing was designed and built to be identical to the Nylon one, the variation in the material properties of the fabric results in the warping of this wing post-inflation, which induces a spanwise twist distribution in the jig shape, along with minor variations in the spanwise camber distribution. Figure 2 shows the wing spanwise twist and max camber distribution as a percentage of local section chord length for both wings on inflation. As can be seen, the camber is 1% or lower along the wing span. Figure 3 illustrates the design NACA 0015 airfoil shape and the realized profiles post-inflation for both wings. Consistent with the literature, inflation of the wing results in a reduction in the wing chord length followed by an increase in the wing thickness.

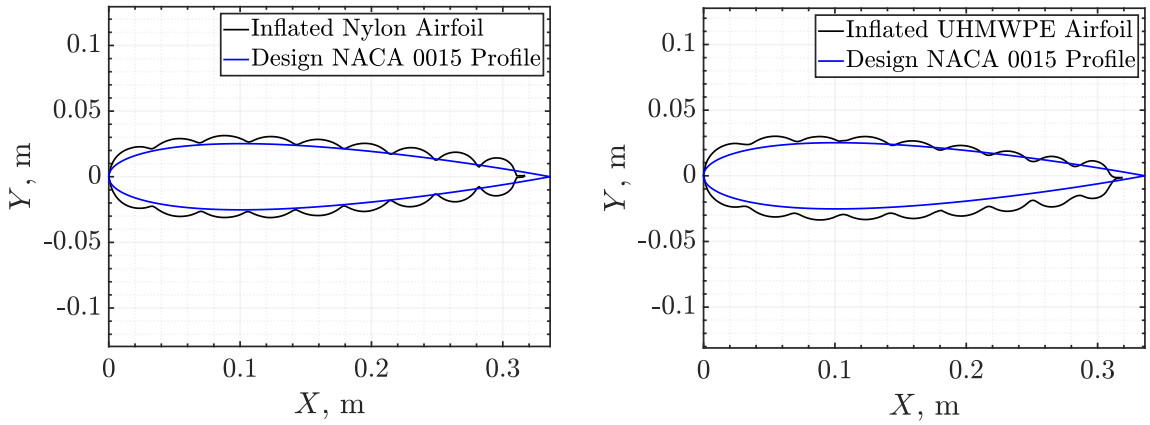

(a) Nylon Wing **(b) UHMWPE Wing**

Fig. 3 Design Airfoil Profile vs Inflated Airfoil Profile

For 3D photogrammetry measurements, over 100 high contrast markers were non-uniformly placed on both inflatable wings and the aluminum mount surfaces. The size of these markers was chosen to provide an accuracy of ±44 µm for out-of-plane displacements and ±14.6 µm for in-plane displacements. For monitoring the dynamic behavior of the wing, two ADXL 335 accelerometers were placed in the channels where the 2nd and 8th baffles are located. An inflation valve is placed between the seventh and eighth baffle (see Fig. 1), which allows for inflating the wings up to a tested limit of 3 psig using a commercially available air pump. The wires for the accelerometers are routed via these channels between the bumps through the mount along with the tubing for the wing inflation.

A clear plastic film, 0.02 mm in thickness, is shrink-wrapped onto the wings to act as a skin to improve the aerodynamic shape and avoid some of the drawbacks associated with "bumpy" inflatable wing sections discussed in Section I. Additionally, this "skin" also protects the accelerometers, wires, and high contrast markers, when the wind tunnel tests are underway. The mid-span cross-section of this "bumpy" airfoil shape with the skin from the nylon wing is shown in Fig. 4. Three tabs with eyelets for connecting tethers to the inflatable wings, also built from a UHMWPE

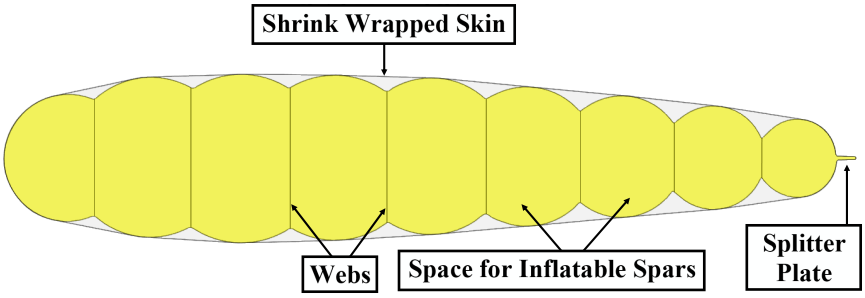

Fig. 4 Nylon Inflatable Wing Cross-Section With Skin

fabric, are attached to the wing surface using epoxy adhesive (see Fig. 5). Two of these tabs are attached at the leading and trailing edges of the wings at ~ 1.5 in. (38 mm) inboard from the wing-tip. The third tab is fixed at the leading edge of the wing at a location ~ 10.5 in. (266 mm) inboard from the wing-tip.

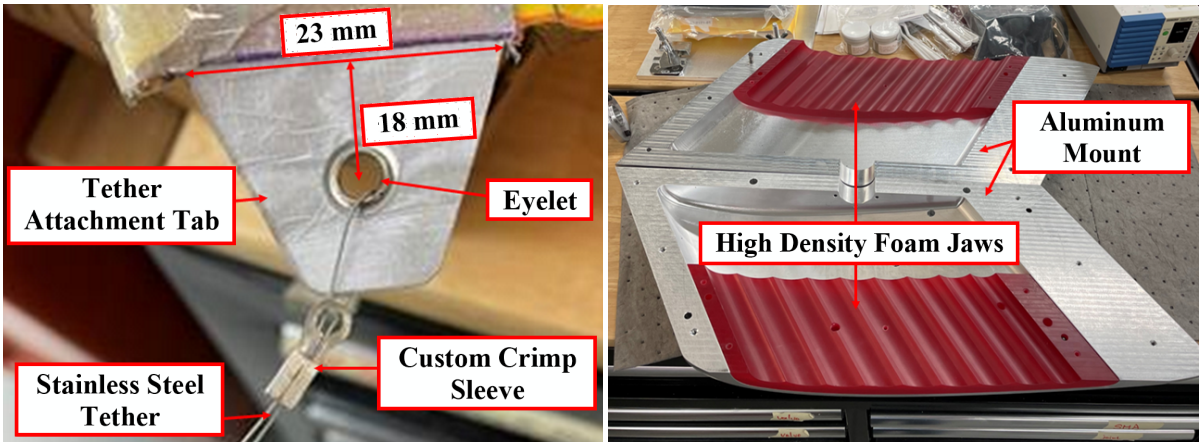

(a) **(b)**

Fig. 5 (a) Tab for Tether Attachment to the Wing and (b) Internal Construction of the Aluminum Mount

An aluminum mount, using the same NACA 0015 airfoil profile as the inflatable wings, was built to support these wings in the wind tunnel and establish a cantilever boundary condition (see Fig. 5). The mount is built in two halves that are bolted together. The holes for these bolts on the mount's outer surface are covered with tape before testing to avoid flow over open cavities. Custom jaws, built using high-density polyurethane foam material (see Fig. 5), are used to fit the inflatable wings inside the mount. The wings are bonded to these jaws using an epoxy adhesive. The bonding strength of the adhesive has been tested and found to be capable of withstanding loads on the wings up to ~ 400 N. The mount is built with an opening at the base to connect the test article to a six-axis force and moment sensor. A hollow cylindrical aluminum adapter, with 120° flats, connects the force and moment sensor to a 3-jaw rotary chuck below the wind tunnel test section floor. The location of this adapter shaft is chosen such that it aligns with the inflatable wing root quarter-chord location. This shaft is also used to route the inflation tube and the accelerometer wires below the test section floor to their respective data acquisition/monitoring instrumentation.

The wing and mount are swept back by 30°, and the reference span and chord of the mount are 0.26 m and 0.6 m, respectively. For the inflatable wings, the reference span is 1.06 m by aerodynamic convention (this is lower than the actual wing span length due to the 30° sweep), and the reference chord is 0.31 m (this is taken chord-wise, i.e., not along the flow direction). The decision to sweep the wing was necessitated to delay the divergence speed of the wing, based on some of the preliminary studies conducted by Zhao et al. [40]. The wing and mount are positioned at a 2.5° angle of attack to the wind tunnel flow direction. The wings are inflated to 2.5 psig internal pressure. For a comparison of the role that the fabric material plays in the aeroelastic performance of the wing, an identical setup was used for the UHMWPE wing. Additional details of the Nylon 200D inflatable wing test article design are also given by Zhao et al. [40], while some of the testing details and preliminary results have been discussed previously by Desai et al. [41]. Figure 6 shows the test article, along with its various features, mounted inside the wind tunnel.

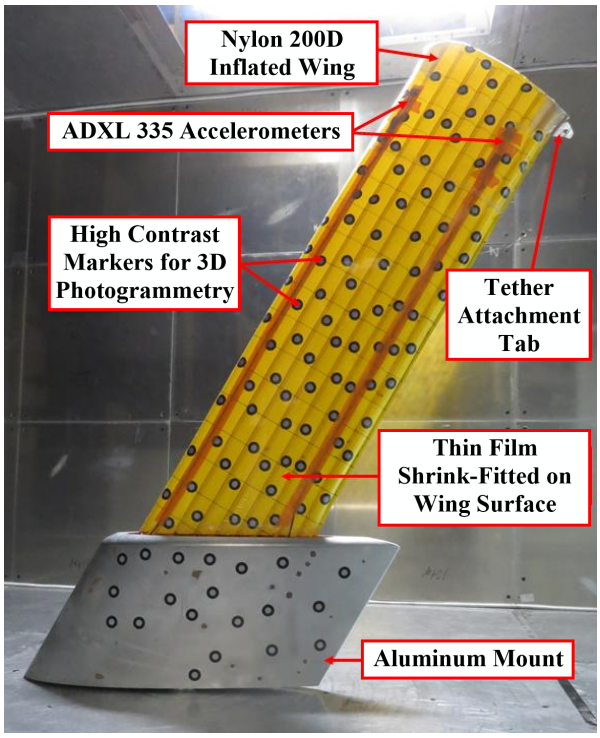

Fig. 6 Assembled Wing and Mount in the Wind Tunnel Test Section

C. Experimental Setup and Wind Tunnel Instrumentation

Inside the test section, the test articles were mounted 3.56 m downstream of the inlet. The angle of attack of the test article was chosen such that the suction side of the wing and mount face the port side wall (to the left when facing the inlet). The six-axis force and moment sensor mentioned in the previous section is a pancake-type sensor from JR3. It has a nominal accuracy of ±0.25% of the full-scale measurement. The full-scale force measurement capacity along the sensor X and Y axes are 400 N, while along the sensor Z axis is 800 N. For the moment measurements,

the full-scale capacity is 50 N·m for all three axes. To compute the forces and moments illustrated in this article, the measurements obtained from the JR3 sensor are rotated so as to align the coordinate axes with standard aerodynamic conventions for lift, drag, and side force in a standard right-handed coordinate system. It must be noted that this force and moment sensor yields the total forces and moments on the wing and the mount after accounting for the force and moment components carried by the tether in each of the test configurations.

The tethers used for these wind tunnel tests were 0.02 inch (0.51 mm) diameter 316 stainless steel wires. They were crimped by means of custom crimping sleeves onto the attachment tabs on the wings. Similarly, they were connected to M8 eye bolts at the other end. A custom 2 ft. $\times$ 2 ft. (0.61 m $\times$ 0.61 m) aluminum panel for the starboard side wall was built with a 7.54 in. $\times$ 6.85 in. (19.15 cm $\times$ 17.40 cm) cutout for letting the tethers through for attachment on the starboard side wall. Tether attachment assemblies were designed and built from 1.5 in. $\times$ 1.5 in. (38.1 mm $\times$ 38.1 mm) T-slotted framing and attachments for all the tether attachment configurations. In addition to these, 3D printed parts, built using a micro-carbon-fiber-filled nylon composite material, were designed for housing load cells for tether tension measurement and connecting them to the T-slotted framing assembly. These parts were designed to house the load cells such that their measurement axis is oriented along the direction of the tether to ensure tension measurement and not just a component of the force along a given direction. Figure 7 illustrates this assembly for the various tested tether attachment configurations. These configurations and the test plan are discussed in the next section.

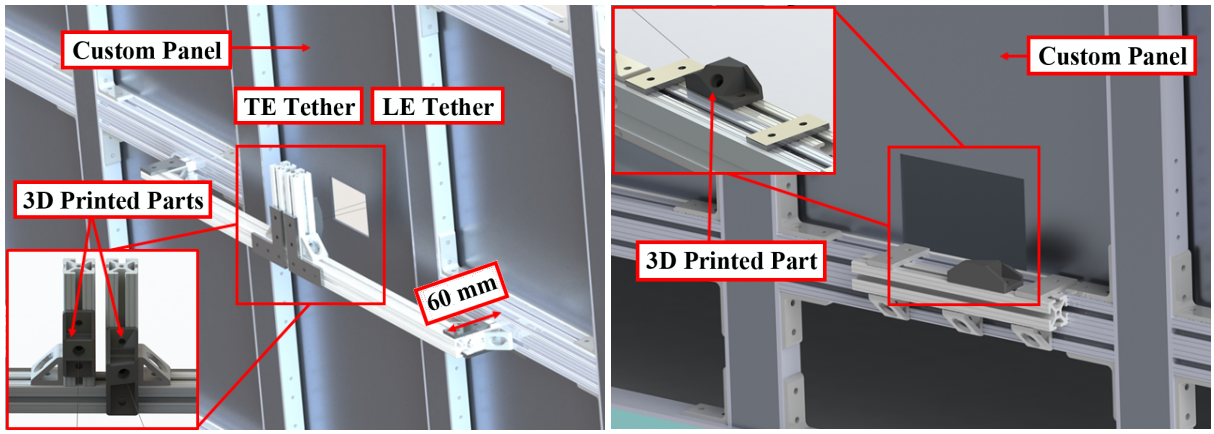

Fig. 7 Tether Attachment Assembly for (a) First Two Configurations and (b) Third Configuration

The load cells used were a single-axis Kyowa LUR-A-100NSA1 load cell with a rated capacity of ±100 N and a single-axis Kyowa LUR-A-50NSA1 load cell with a rated capacity of ±50 N. The combined error of these load cells is ±1.0% of the rated output. The M8 eye bolts discussed earlier were bolted onto these load cells. During the test, the load cells were zero-balanced without the tether to take into account any tether pre-tension. Care was taken to ensure minimal to no pretension in the tethers for all test configurations by monitoring the load cell readings during the tether attachment procedure. For logging the signal from these tension measurement load cells as well as the

accelerometers, a Kyowa EDX-100a-4H data logger was placed below the wind tunnel test section floor. The load cells for the tension measurements were routed from behind the starboard side wall to the data logger via 10 ft. (3.05 m) long data cables. The data logger was connected to a computer placed in the port side anechoic chamber for recording the data using its accompanying software. A National Instruments USB-6211 DAQ was used to supply 5V DC power to the accelerometers. The internal inflation pressure of the wing was monitored before, during, and after each test run with an analog pressure gauge attached to the inflation tube below the test section floor.

For the 3D photogrammetry measurements, a custom 0.5 inch (12.7 mm) thick acrylic panel of dimensions 2 ft. $\times$ 4 ft. was designed and built for optical access to the test section from the port side anechoic chamber. Some small distortion from the acrylic panel for the displacement measurements is expected, but the magnitude of this uncertainty remains to be quantified. Dong and Pan [42] discuss an approach to account for optical distortion due to such a glass panel and the uncertainties involved. The 3D photogrammetry system is a commercially available high-speed camera system designed by GOM [43], called ARAMIS HS. The system consists of two 1.3 MP cameras (with 24 mm lenses) whose alignment was calibrated before the test using an accompanying 1.4 m calibration cross. Due to the size of the test article, the distance between the two cameras was kept at 688 mm, and the distance between the cameras and the test article was kept at 1850 mm, as recommended by the manufacturer. The shutter speed of the cameras necessitates the use of high-frequency LED lights to let enough light through the camera lenses for photogrammetry measurements.

The presence of the thin clear film on the wing surface results in a lot of reflected light from the aforementioned LEDs, which requires the use of polarized lenses to obtain a clearer picture. The camera height, the LED placement, and the lighting were adjusted before testing to ensure that a maximum number of markers were detected during the test. The accompanying computer system and PONTOS software [43] were used to check and adjust the lighting, record displacement-field measurements, and partially post-process the test data. Since not all markers are detected during a test, non-uniform spacing for the placement of these high-contrast markers on the inflatable wings was a prudent choice. Interestingly, the choice of fabric color had an effect on the reflection from the wing during the test and consequently had a noticeable impact on the number of markers detected. As a result, it may be reasonable to conclude that the choice of fabric/wing color can also impact the uncertainty in the displacement measurements from the photogrammetry system, depending on the lighting conditions in a given test section.

The test section temperature was measured using an Omega Thermister type 440004, which has an accuracy of $\pm 0.2^{\circ}$K. The ambient pressure in the vicinity of the test section was measured using a Validyne DB-99 barometer with a resolution of 0.05 psig. Concurrently, the dynamic pressure in the test section was measured using a Datametrics Model 590D transducer with an operating range of 10 Torr (1333 Pa) [35].

For the Pitot and static pressure profile measurements in the wake of the wing, a wake rake consisting of 117 total pressure probes spanning 99% of the test section width was installed near the exit of the test section. Seven intermittent static pressure probes are also present to assess if the static pressure has relaxed in the wake of the model. The assembled

wake rake is shown in Fig. 8, and it has been used in the past for various applications [44, 45]. The rake can traverse along the height of the test section from 12 inches (~ 30 cm) off the floor up to 12 inches (~ 30 cm) from the ceiling. The probes on the rake are connected to four DTC ESP 32HD pressure scanners which are capable of measuring 2.5 psig differential pressure with a full-scale accuracy of ±0.05%. The Pitot pressure coefficient discussed here is given by Equation 1. The typical uncertainty in the total pressure coefficient obtained from the wake survey is about ±0.005.

$$C_{p_0} = \frac{P_0 - P_\infty}{\frac{1}{2}\rho U_\infty^2} \tag{1}$$

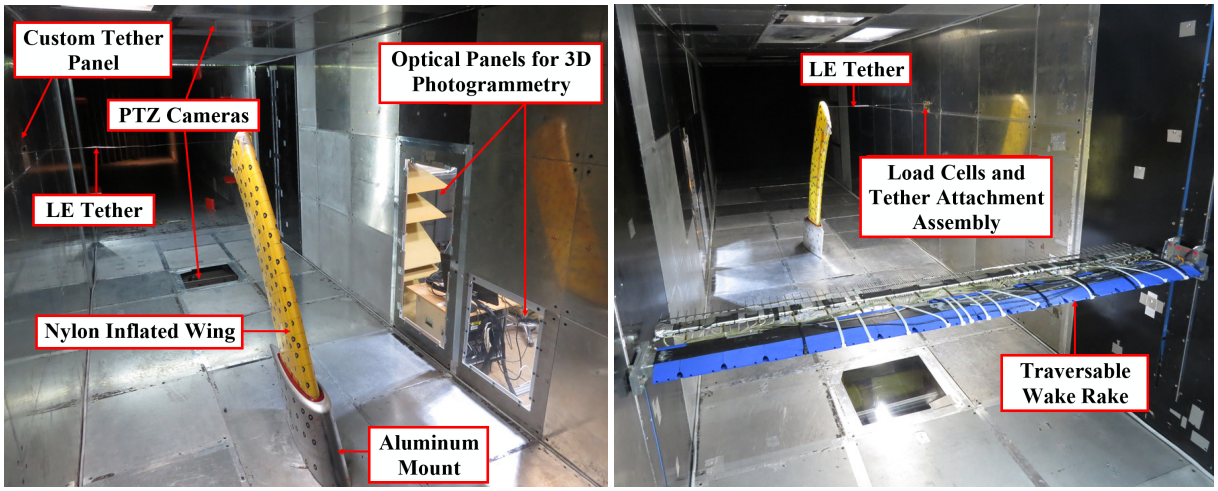

(a) (b)

Fig. 8 (a) Assembled Nylon 200D Wing and Mount and (b) Wake Rake Assembly

The tests were conducted for three different configurations for each wing. Each configuration is determined by the location of the tether attachment on the wing as well as on the tunnel side wall. The first configuration involves a single tether connected perpendicularly from the wing-tip leading edge to the tunnel starboard side wall. The second configuration involves an additional tether attached from the wing-tip trailing edge to the tunnel starboard side wall such that it intersects the leading edge tether at a virtual bridle point 12 inches behind the wall. The third configuration involves a single tether attached from the 77% span location at the leading edge of the wing to a point close to the tunnel floor on the starboard side wall. This third configuration is most representative of an inflated wing kite. All three assembled tether attachment configurations are shown in Fig. 9 for the Nylon wing and in Fig. 10 for the UHMWPE wing. For ease of reference in the coming sections, these configurations have been coded as shown in Table 2.

D. Test Plan

The test plan involved varying the tunnel speed from 15 – 32.5 m/s in 2.5 m/s increments. Forces and moments, tether tension data, photogrammetry data, and accelerometer data were logged for each of these speeds. The tether

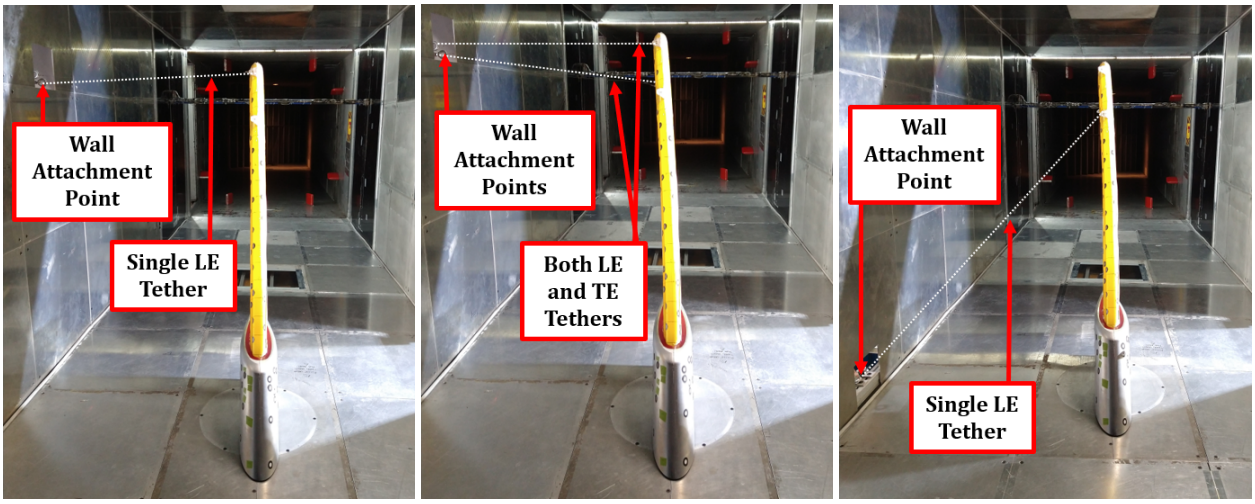

(a) NYL100LE **(b) NYL100LETE** **(c) NYL77LE**

Fig. 9 Tether Attachment Configurations for the Nylon Wing

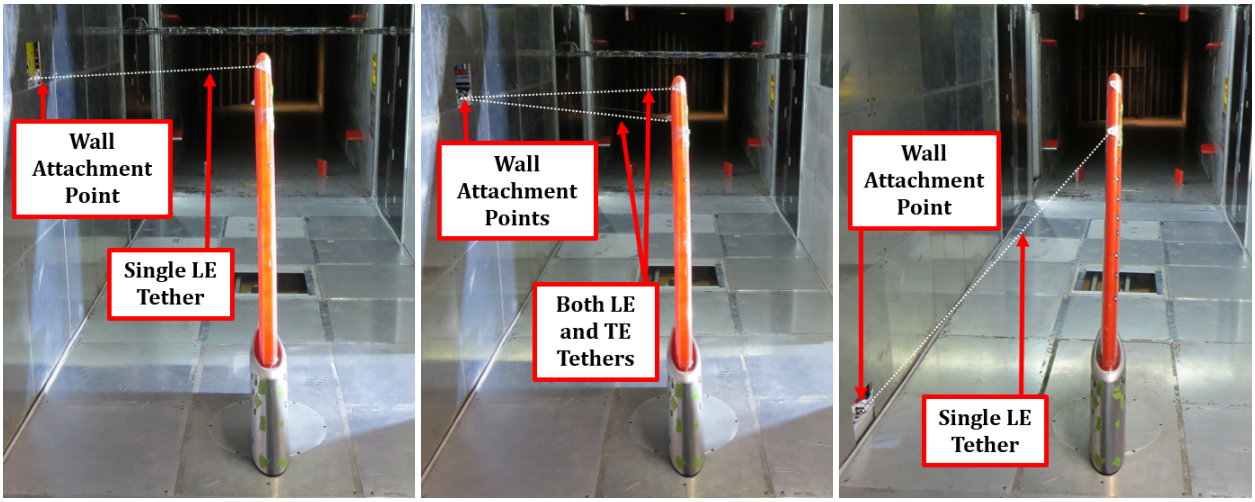

(a) DYN100LE **(b) DYN100LETE** **(c) DYN77LE**

Fig. 10 Tether Attachment Configurations for the UHMWPE Wing

Table 2 Nomenclature for the Various Tether Attachment and Testing Configurations

Tether Attachment Configuration	Nylon 200D Wing	UHMWPE Wing
Single LE Tether at Wing Tip	NYL100LE	DYN100LE
Both LE and TE Tethers at Wing Tip	NYL100LETE	DYN100LETE
Single LE Tether at 77% Span	NYL77LE	DYN77LE

tension data and accelerometer data collected from the data logger were sampled at 2 kHz for 60 seconds. The data from the six-axis force and moment sensor was sampled at 5 kHz for 10 seconds. The data collection at each wind tunnel speed was time-synced. The static aeroelastic deformation measurements at each speed were computed from 10

instantaneous images taken over 10 seconds from the 3D photogrammetry system.

The wake surveys, using a traversable wake rake, were conducted at a speed of 27.5 m/s. Each wake survey took approximately one hour to complete, with pressure data collected for about 30 seconds at each vertical location of the rake. The full span of the rake traverse was used with a vertical resolution of 0.5 inch ($\sim$ 1.27 cm) approximately in the wake of the wing tip (between vertical positions of 42 inches (106.68 cm) to 60 inches (152.40 cm) off the floor) and a resolution of 1.0 inch (2.54 cm) for the rest of the data points, totaling 67 vertical measurement locations. In addition to the wake survey, the wake rake was also installed at the mid-height of the wind tunnel during the initial speed runs. During these runs, the rake was utilized to collect pressure data at this fixed vertical location at each speed. This allows for assessing the variation in the wake profiles due to static aeroelastic deformations. For the static aeroelastic deformation measurements during the wake surveys at 27.5 m/s, 10 images were taken over 10 seconds every 15 minutes to obtain 40 images for computing the static aeroelastic displacement field.

III. Results and Discussion

The static aeroelastic deformation results are presented first. These are then followed by the spanwise twist distribution. These provide insight into the aerodynamic shape of the wing and the effective angle of attack and, as a consequence, indicate the expected behavior of aerodynamic force and moment measurements as the dynamic pressure is varied. These forces and moments are presented next, followed by the pressure measurements in the wake of the wing. These measurements are time-synced to avoid uncertainties stemming from temperature and time variability effects on this fabric-based wing. This data set is designed to provide a comprehensive understanding of the aerodynamics of the test article, stopping short only of flow visualization enabling measurements in the wind tunnel.

A. Static Aeroelastic Deformations

Static aeroelastic deformations were obtained using the 3D photogrammetry system at a non-uniform set of discrete high-contrast marker locations on the wing. The marker coordinates were transformed from the photogrammetry system coordinate frame to the real-world coordinate frame of the wind tunnel. To that end, a reference marker on the test article, which remains stationary during testing, is necessary to orient the coordinate frame of the photogrammetry measurements correctly. Inaccuracy in the measurement of the reference marker location (measured relative to the mount base leading edge before testing) can lead to uncertainties in the static aeroelastic measurements, which can propagate through the displacement field generation process. This orientation of the coordinate frame was done while post-processing the raw photogrammetry data after the wind tunnel test. The photogrammetry system outputs the coordinates of the remaining markers relative to this measured reference marker.

Before the wind tunnel was started, an image of the wing was taken with the photogrammetry cameras. This image then serves as a reference for computing the displacement field for the wings during a given configuration run at each

wind tunnel speed. An average of the displacement field computed from 10 images at each wind tunnel speed is given in this section. Some preliminary post-processing is conducted in the software accompanying the photogrammetry system, which involves discarding data points with measurement errors due to reflections from the LEDs or other distortions. An in-house post-processing code was used to add and automate some additional transformations required to accurately associate the measured deformations from the photogrammetry system to real-world coordinates. From all the measurements, the in-plane deformations (δ_X and δ_Y) are negligible, while the out-of-plane measurements (δ_Z) dominate. The sign convention is chosen such that positive out-of-plane deformations are taken to be out of the page.

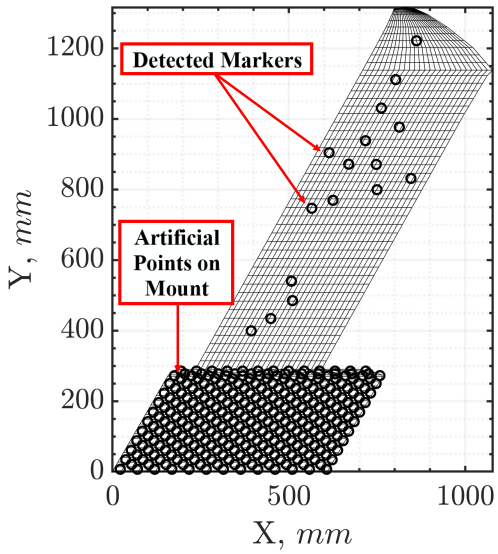

Fig. 11 Example of Detected Markers from the Photogrammetry System for a NYL100LETE Case at 32.5 **m/s**

Importantly, not all markers present on the wing are detected during a given run. Additionally, the detected markers may vary at different wind tunnel speeds during a run depending on if the lighting and conditions change substantially. This may happen if the deformations are sufficiently large that they alter how the light from the high-frequency LEDs is reflected off the wing surface and refracted through the optical access panel. Care was taken to ensure the camera system stays rigid and does not move during the run, as this can render the measurements unusable for obtaining the displacement field. As may be evident, both the reference image and the images at each speed during the run must detect the same markers to compute the displacements. Figure 11 shows an example of the detected markers for the NYL100LETE case at a wind tunnel speed of 32.5 m/s. The markers are aligned with a grid associated with the inflatable wing planform. As seen from the figure, few markers are detected during a given run. Consequently, the displacements must be interpolated and extrapolated to obtain a continuous displacement field on the wing.

For interpolating/approximating this scattered multidimensional deformation data obtained at discrete marker locations to the inflatable wing, a piecewise continuous radial basis function (RBF) based interpolation/approximation code is leveraged [46]. The RBF kernel used corresponds to the thin plate spline approach *sans* the additional constraints

typically used to augment the RBF method prevalent in the applied aeroelasticity community. Depending on the number of detected markers and the choice of the RBF kernel, some differences in the displacement field on the wing may be observed. Since this is not the focus of this paper, it has not been discussed in further detail. Still, it can serve as an avenue for future research in applying scattered interpolants for experimental displacement field measurements. This RBF code is coupled with the measured displacements from the photogrammetry system and point cloud data from a scan of the inflatable wing geometries. The point cloud is obtained using a state-of-the-art ARAMIS scanner [47].

This point cloud is converted into a surface triangulation in the standard tesselation language (STL) format and then cleaned and smoothed in Autodesk® Meshmixer [48]. The coordinates from the surface triangulation are extracted while not altering the connectivity matrix and associated with the measured displacements from the photogrammetry system to build the interpolation/approximation function. Once this interpolant has been constructed, the displacement field for the inflatable wing is obtained for a given case. The deformed inflatable wing geometry is then written in the STL format, which can be easily read into any Computer Aided Design (CAD) software. These STL format geometries are also used to visualize the displacement fields for all cases.

For both wings, the measured data points from the photogrammetry system were placed at the mid-plane of the test article while also following the warping induced in the UHMWPE wing. The reason for this is that measured displacements are initially associated with the suction side of the wing, which leads to the RBF code computing non-physical deformations of the three-dimensional wing geometry. The spanwise twist distribution was obtained chordwise instead of streamwise for ease of interpretation of the spanwise twist distribution for this 30° swept wing. For this purpose, points were sampled at the wing leading and trailing edges after computing the displacement field. The spanwise stations for the twist distribution plots were chosen to be at the mid-chord point of an imaginary line joining the leading and trailing edge points. The elastic twist angle at each station is then computed as:

$$\theta_e = \arctan\left(\frac{Z_{LE} - Z_{TE}}{\sqrt{(X_{LE} - X_{TE})^2 + (Y_{LE} - Y_{TE})^2}}\right) \tag{2}$$

Now that the static aeroelastic displacement data acquisition and post-processing methodology have been established, the results are presented for the Nylon and UHMWPE wings, respectively. The displacement profiles for each configuration for the Nylon wing are illustrated in Fig. 12. The NYL100LE and NYL100LETE results are presented for a wind tunnel speed range of 15.0 – 32.5 m/s, while the NYL77LE case results are presented for wind tunnel speeds ranging between 15.0 – 27.5 m/s. For ease of comparison, the color bar scales are kept the same for all cases. The displacements illustrated are the out-of-plane ones since, as mentioned previously, the in-plane displacements were found to be negligible. The spanwise twist distribution plots for the Nylon wing cases are illustrated in Fig. 13. As with all the cases in this study, the out-of-plane displacement profiles illustrate an increase in displacement magnitudes as the wind tunnel speed (and hence dynamic pressure) increases.

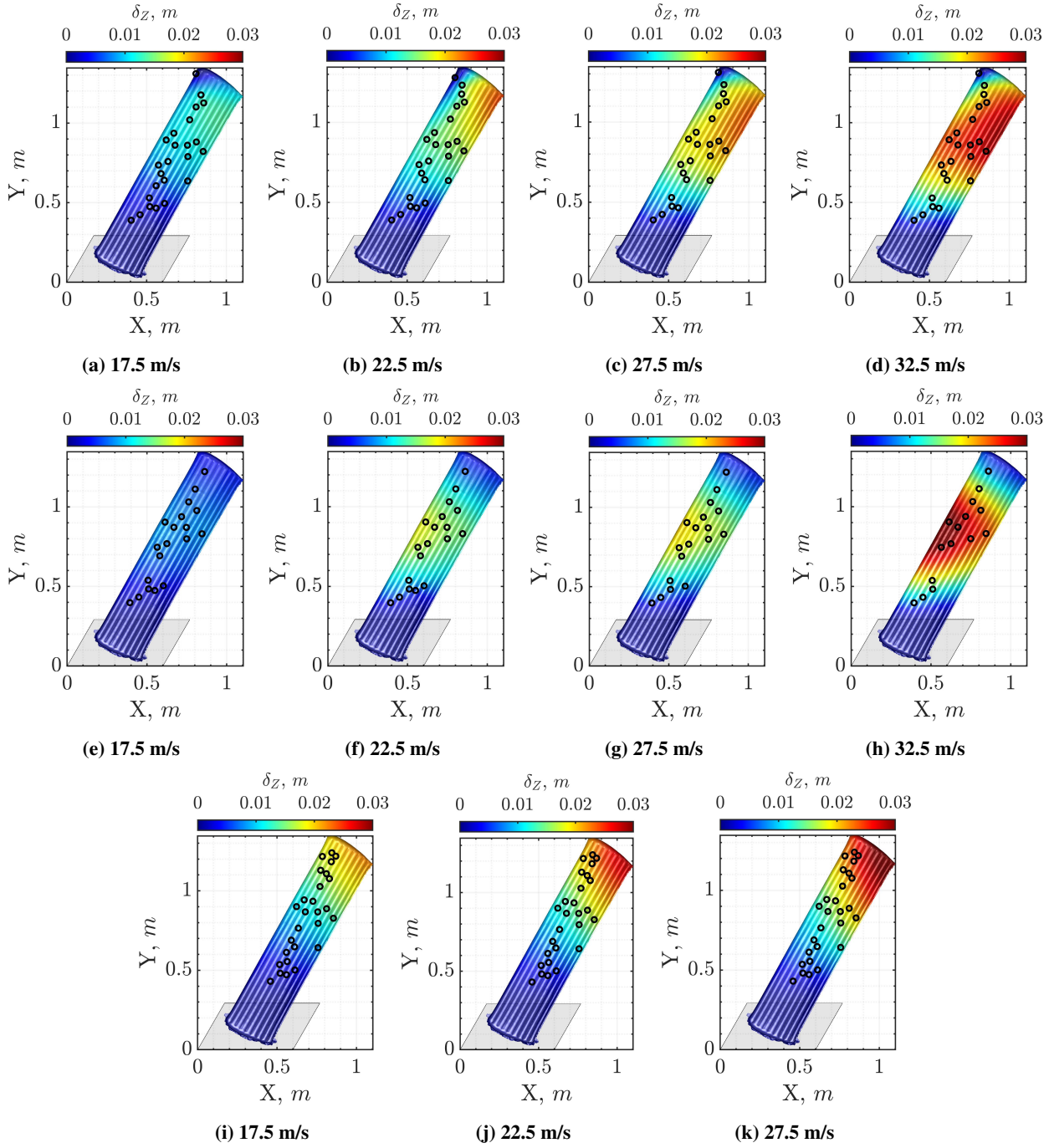

(a) 17.5 m/s **(b) 22.5 m/s** **(c) 27.5 m/s** **(d) 32.5 m/s**

(e) 17.5 m/s **(f) 22.5 m/s** **(g) 27.5 m/s** **(h) 32.5 m/s**

(i) 17.5 m/s **(j) 22.5 m/s** **(k) 27.5 m/s**

Fig. 12 Out-of-plane Static Aeroelastic Deformations (δ_Z) for the NYL100LE Case (a – d), the NYL100LETE Case (e – h), and the NYL77LE Case (i – k)

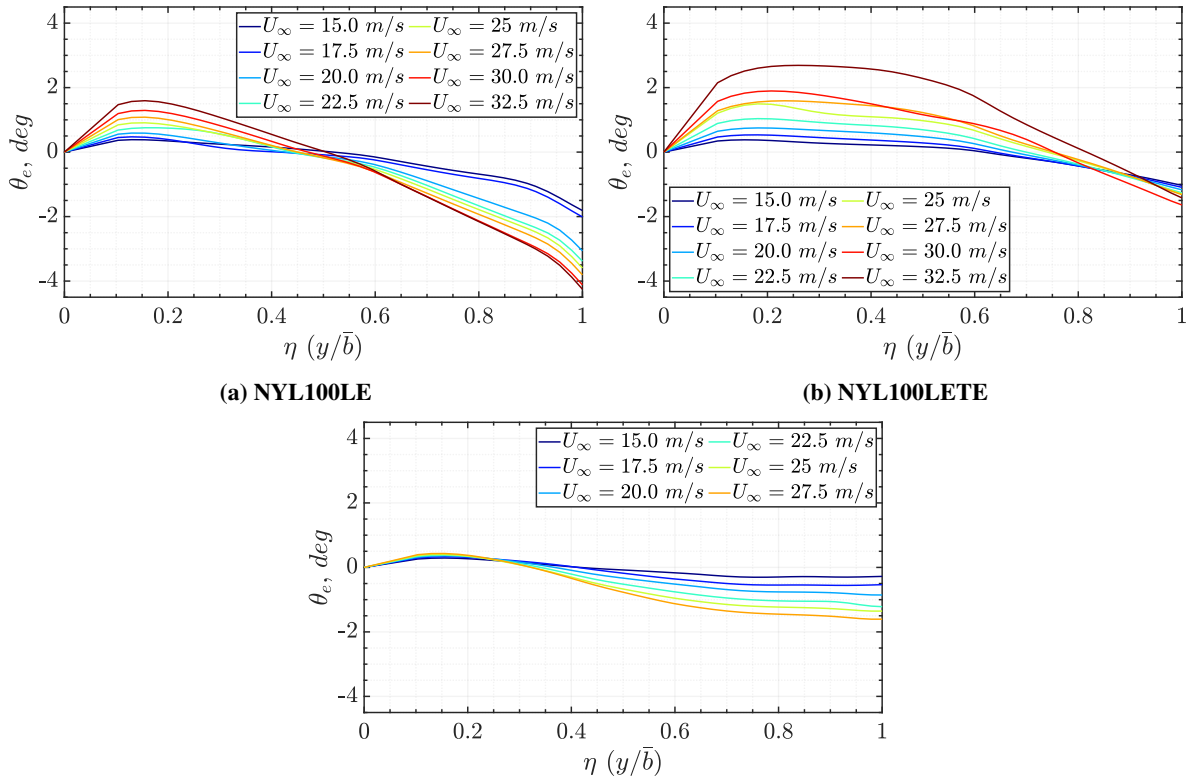

(a) NYL100LE

(b) NYL100LETE

(c) NYL77LE

Fig. 13 Spanwise Elastic Twist Distributions for the Nylon Wing Cases

For the NYL100LE case, most of the displacements are concentrated towards the wingtip trailing edge. The maximum displacement for this case is ~ 0.035 m at 32.5 m/s with a maximum negative twist of $\sim -4°$. As a result of these displacements, increasingly negative twist angles near the wingtip and positive twist angles near the wing-mount junction are computed with increasing wind tunnel speed. The NYL100LETE case results in a remarkably different displacement profile with negligible out-of-plane displacements towards the wingtip and a positive twist angle in the mid-section of the wing. The maximum out-of-plane displacement for this case is also ~ 0.035 m at 32.5 m/s with a maximum positive twist angle of 2.75°. The NYL77LE case exhibits a negative spanwise twist resulting in a decrease in the effective angle of attack. The maximum out-of-plane displacement for this case is ~ 0.04 m at 27.5 m/s, which is significantly greater than the other two Nylon wing cases. As is evident when looking at Figs. 12 and 13 together, this case results in a lot more bending in the wing than twist. These flexibility effects due to the tether attachment configuration result in very different aerodynamic profiles for the same wing.

Next, we examine the static aeroelastic displacement measurements obtained from the UHMWPE wing cases. Similar to the Nylon wing, the out-of-plane displacements for the UHMWPE wing for the various tether attachment configurations are illustrated with increasing wind tunnel speeds (see Fig. 14). As noted in Section II.C, the warpage in the UHMWPE wing on inflation induces a spanwise twist in the wing and some camber. Hence, the UHMWPE wing is

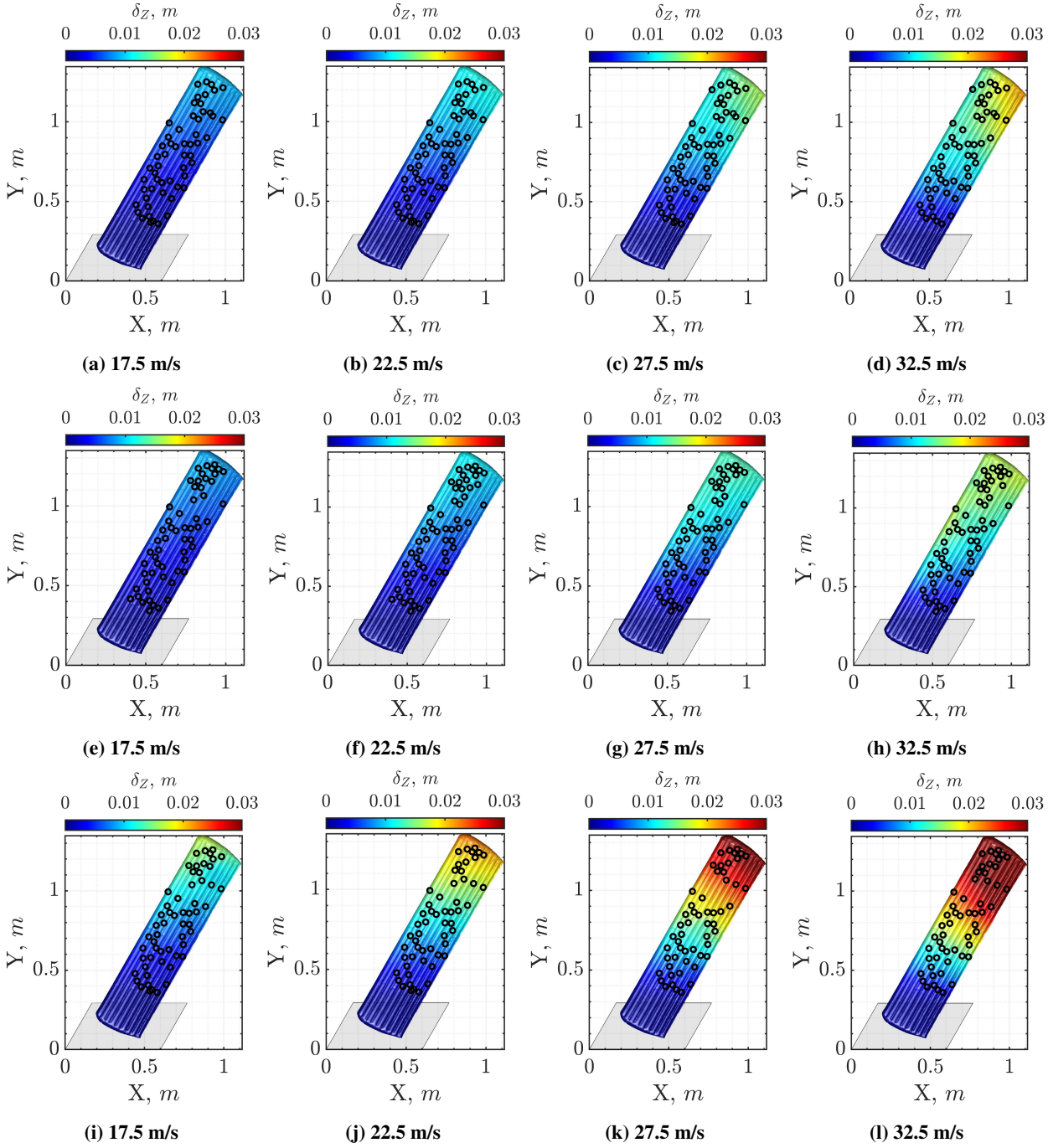

(a) 17.5 m/s **(b) 22.5 m/s** **(c) 27.5 m/s** **(d) 32.5 m/s**

(e) 17.5 m/s **(f) 22.5 m/s** **(g) 27.5 m/s** **(h) 32.5 m/s**

(i) 17.5 m/s **(j) 22.5 m/s** **(k) 27.5 m/s** **(l) 32.5 m/s**

Fig. 14 Out-of-plane Static Aeroelastic Deformations (δ_Z) for the DYN100LE Case (a – d), the DYN100LETE Case (e – h), and the DYN77LE Case (i – l)

not symmetric on inflation. This spanwise camber and twist (θ_t) induced due to warpage have been extracted from the scanned geometry of the UHMWPE wing and are as illustrated in Fig. 2.

To place the measured displacement data points from the photogrammetry system at the midplane of the wing, this warpage-induced twist has to be accounted for before utilizing the RBF interpolant to obtain the displacement field for this wing. Consequently, the displacement profiles illustrated in Fig. 14 are relative to this warped wing. Figure 15 shows the spanwise variation in the elastic twist angles for each of these configurations with variation in the wind tunnel speed. These twist angles are computed relative to the warped wing and do not include the warpage-induced twist angles discussed earlier. As shown in Fig. 15, the magnitude of these twist angles is very small, with a maximum twist angle of $\sim 2^\circ$ for the DYN100LETE case at 32.5 m/s. This makes it challenging to identify trends for this wing since, at lower wind tunnel speeds, these angles likely lie in the uncertainty bounds introduced due to the RBF interpolant.

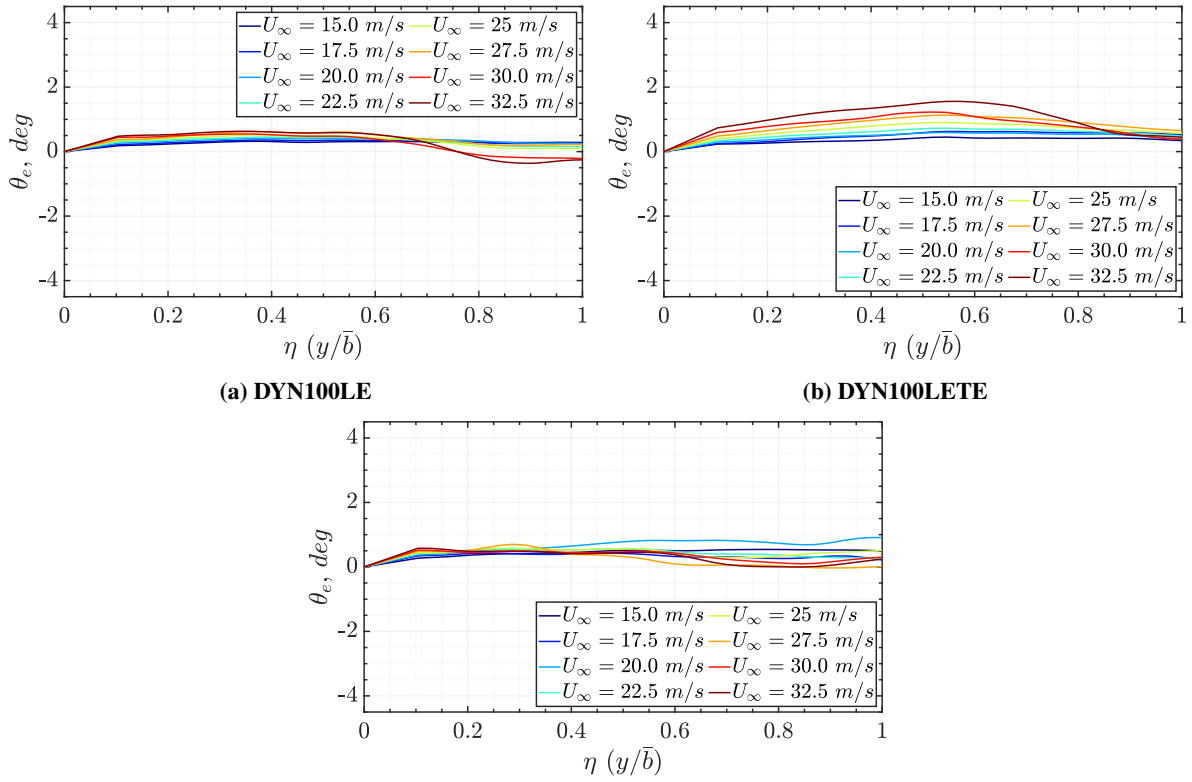

(a) DYN100LE

(b) DYN100LETE

(c) DYN77LE

Fig. 15 Relative Spanwise Elastic Twist Distributions for the UHMWPE Wing Cases

Figure 14 illustrates the out-of-plane displacements on the UHMWPE wing for the three tether attachment configurations with varying wind tunnel speeds. The trends in the displacement field for these cases are similar to those observed in the nylon wing, albeit the magnitudes of these displacements are lower. This is because the UHMWPE wing fabric is much stiffer than the nylon wing fabric, resulting in a much stiffer wing overall. Similar trends for the same configurations across the two inflatable wings indicate some generalizability of the findings from these

measurements, i.e., the single tether configurations introduce increasingly negative twist angles towards the wingtips with increasing wind tunnel dynamic pressures. In contrast, the two tether configurations result in positive twist angles in the mid-section of the wing (see Figs. 13 and 15). As these displacements affect the aerodynamic profile of the wing, identical displacement trends for a given tether attachment configuration across the two wings are expected to yield identical trends in the forces and moments experienced by the wing. However, these trends are also a function of the fabric stiffness and its effect on the wings' response to aerodynamic loading.

B. Forces and Moments

The force and moment measurements on the test article have been aggregated from the single-axis sensors for the tether tension measurements and the JR3 six-axis force and moment sensor at the aluminum mount base. As the wind tunnel runs are conducted, the JR3 sensor measures the forces and moments on the wing and mount. At this time, the tethers carry some of the aerodynamic loads. Hence, the components from these tension measurements have to be accounted for to compute the aerodynamic forces and moments. Coordinate frame transformations are also made to ensure the aerodynamic forces and moments are according to conventions for lift, drag, etc. The JR3 sensor dynamic data were post-processed to exclude the 60 Hz hum from the voltage source using a bandstop filter, and all frequencies over 100 Hz were filtered using a low-pass filter. It must be noted that this filtering has a negligible impact on the mean values. This procedure is repeated for all the force and moment data.

1. Nylon Wing Forces and Moments

Here, the forces and moments on the Nylon wing have been compared for all three tether attachment configurations. As may be evident, the chosen instrumentation for tension, force, and moment measurements is typically such that the maximum measurement capability of the instrument is not exceeded during the test. However, a higher instrument measurement range affects the nominal accuracy of that instrument at lower measurement magnitudes. Furthermore, due to wing flexibility, the aerodynamic loads increase in a non-linear manner with increasing wind tunnel dynamic pressures at a fixed angle of attack. As a result, when compared with a rigid wing of similar dimensions, a higher range of measurement capability is required for the flexible wing, which impacts the uncertainty in measurements at lower wind tunnel speeds and dynamic pressures.

Mean aerodynamic forces and moments for all three tether attachment configurations for the Nylon wing are illustrated in Fig. 16. The error bars indicate a 95% confidence bound on the data. Since the angle of attack for the test article is kept constant while only varying the dynamic pressure, the variations in the forces and moments arise from the wing's flexibility and the various tether attachment configurations. The inclusion of pre-tension also induces an initial deformation in the wing, i.e., variations in pre-tension likely affect the aerodynamic performance. This uncertainty in pre-tension points to challenges in the repeatability of tests for such flexible wings. The displacement field and twist

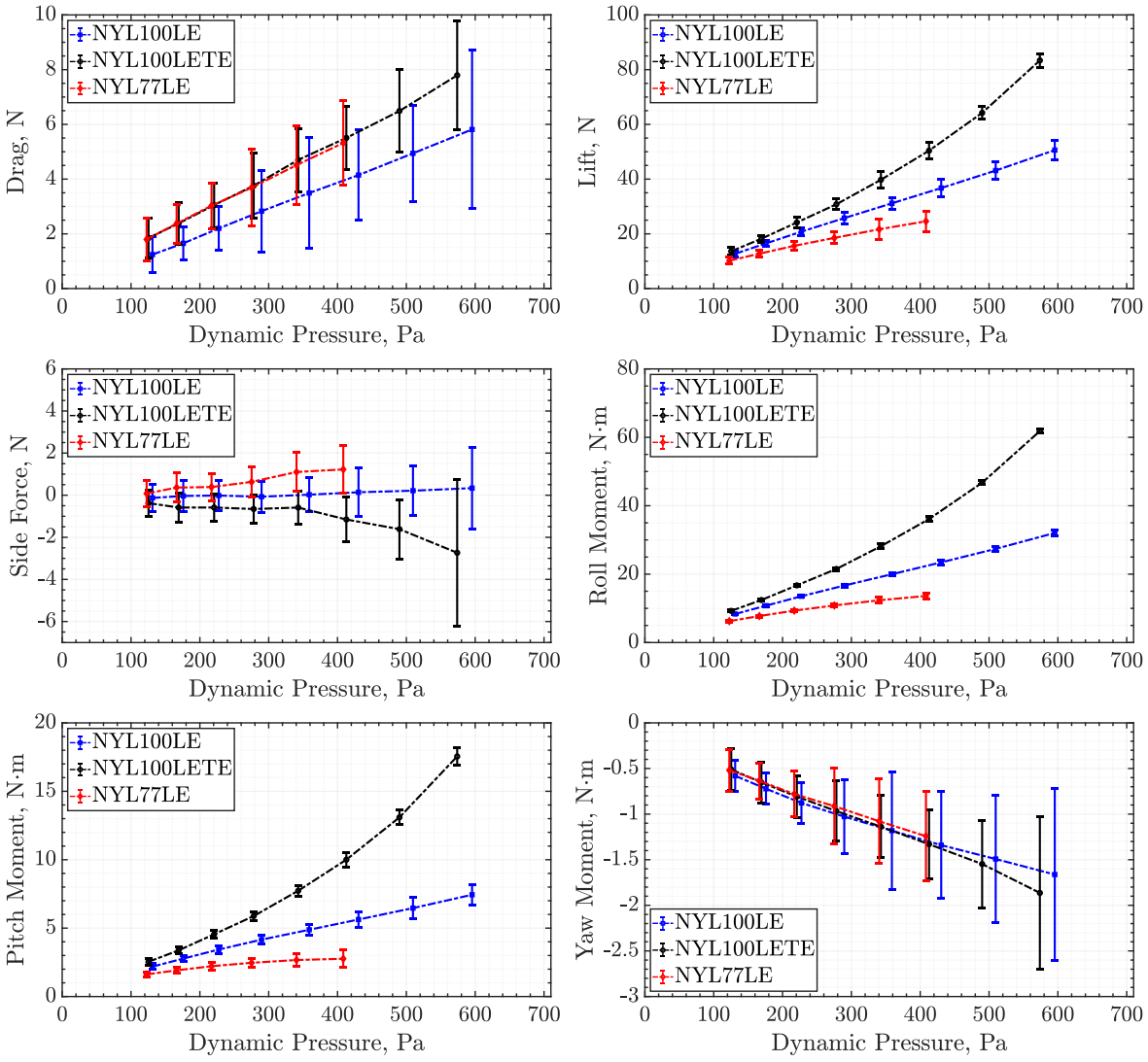

Fig. 16 Comparison of Lift, Drag, Side Force, Rolling Moment, Pitching Moment, and Yawing Moment for All Three Tether Attachment Configurations for the Nylon Wing (Tether Forces Included)

distribution data presented in the previous section provide insight into the expected aerodynamic behavior of the wings. Additionally, the variations in forces and moments are still scaled by dynamic pressure. Hence, to interpret the effect of flexibility on aerodynamics, the changes in the forces and moments with dynamic pressure are to be inferred.

For the NYL100LE case, the lift seemingly increases linearly with dynamic pressure up to a certain point. But, if scaled by dynamic pressure, there is a drop in the lift coefficient at lower speeds due to the development of a negative twist angle towards the wing tip. At higher speeds, the lift coefficient rises, most likely due to the increase in the positive twist in the wing near the wing-mount junction. The NYL100LETE case, on the other hand, sees an increase in the lift coefficient with dynamic pressure as evidenced by the non-linear increase in the lift. This increase is driven by the increase in twist angle in the mid-section of the wing with dynamic pressure, as discussed in the previous section. The NYL77LE case sees a reduction in the lift coefficient with dynamic pressure, as well as the lift magnitude. This is due to the negative twist developing in the wing with increasing dynamic pressure. This case also shows significant bending in the wing towards the wing tip.

The roll and pitch moment trends follow those of the lift for all the cases, as expected. The major inference from these results is that the tether attachment configuration can be tailored to obtain high lift, as in the NYL100LETE case, or can be utilized for load alleviation, as in the NLY77LE case. This identifies a potential for passive aeroelastic tailoring of inflatable wing kites which is crucial for the success of such high-altitude platforms/airborne wind energy systems. The trends in the drag measurements for all three cases were fairly similar, but one must remember that the magnitudes are of the same order as the uncertainty. The expectation from an aerodynamic standpoint is that the drag coefficient should increase as the lift coefficient increases due to the induced drag effect. But, it should also be stated that the negative twist in the wing could induce some separation that could increase the form drag. Hence, the flow field over the wing needs to be probed further for each case to draw a concrete conclusion. Similarly, little can be said about the side force measurements since their magnitudes are of the same order as the uncertainty.

2. UHMWPE Wing Forces and Moments

As discussed earlier, the UHMWPE wing is stiffer and hence, exhibits negligible low-frequency dynamic oscillations during the wind tunnel test. This inference is made from the time-domain force and moment measurements for this wing. Like for the nylon wing, Fig. 17 compares the mean aerodynamic forces and moments for all three configurations of the UHMWPE wing. The trends for each configuration are identical to those observed in the nylon wing. However, the magnitudes of the forces and moments are different owing to the wing fabric materials (discussed in detail in the next section). These trends in the UHMWPE wing also reinforce the conclusions drawn for the various tether attachment configurations from the nylon wing. As in the NYL100LE and NYL77LE cases, the DYN100LE and DYN77LE cases see a reduction in the lift with increasing dynamic pressure. Like the NYL100LETE case, the DYN100LETE case also sees an increase in the lift coefficient with dynamic pressure. These trends also carry over to the roll and pitch moments.

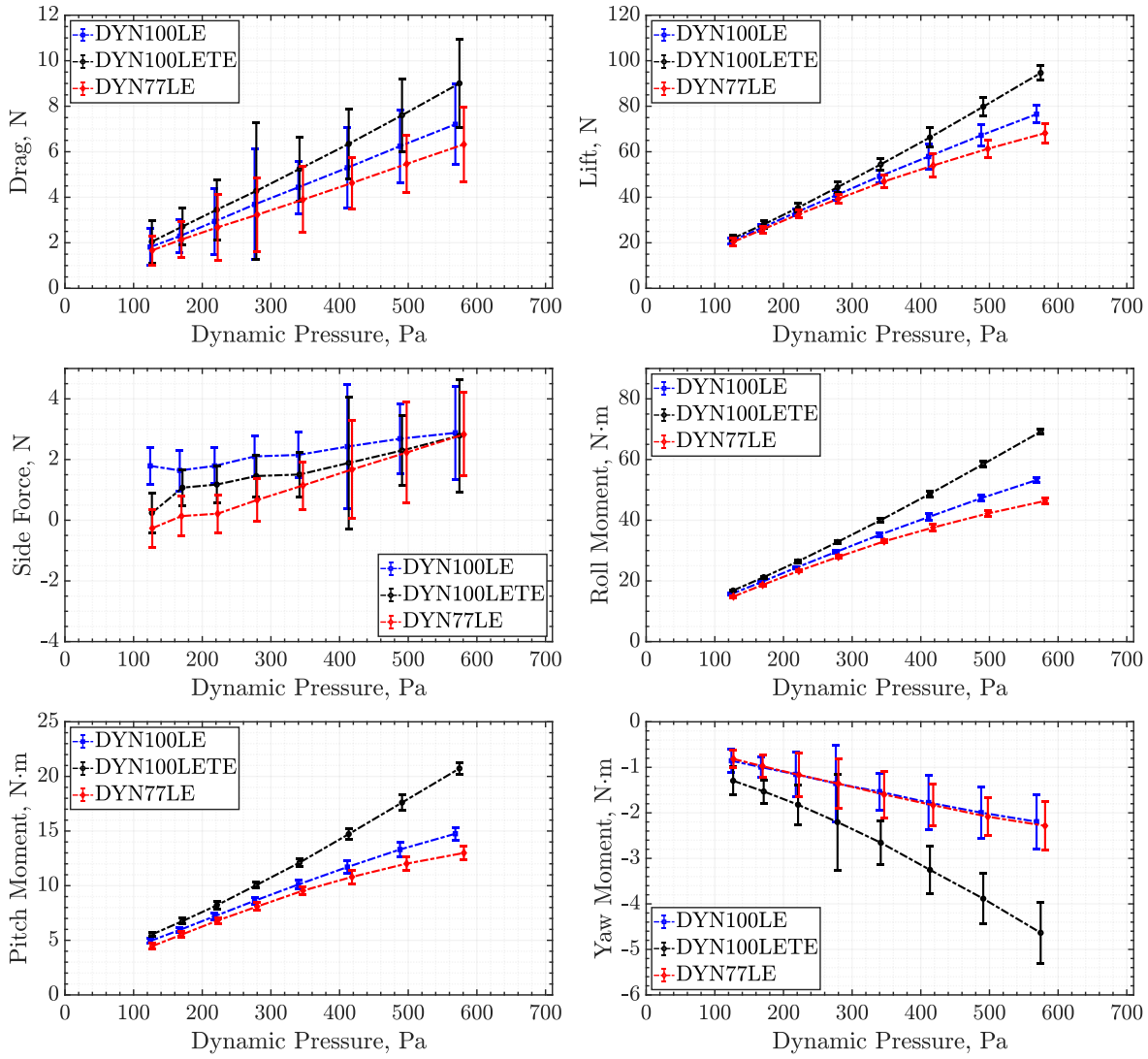

Fig. 17 Comparison of Lift, Drag, Side Force, Rolling Moment, Pitching Moment, and Yawing Moment for All Three Tether Attachment Configurations for the UHMWPE Wing (Tether Forces Included)

Interestingly, the drag data follow the expected trends discussed at the end of Section III.B.1.

3. Comparison of the Nylon and UHMWPE Inflatable Wing Forces and Moments

This sub-section on the comparison of the forces and moments between the nylon and UHMWPE wings serves to provide a contrast in the aerodynamic performance of these wings for identical tether attachment configurations. Hence, the differences noted in these cases arise primarily from the wing fabric material. These comparisons have been illustrated for each of the three tether attachment configurations. Figure 18 compares the forces and moments from the NYL100LE and DYN100LE configurations. A marked difference is observed in the lift generated by the two wings, where the UHMWPE wing generates ~ 40% more lift at a given wind tunnel speed. This large difference is due to the warpage in the UHMWPE wing discussed earlier. The roll and pitch moments follow a similar trend. The UHMWPE

wing experiences more drag due to its much greater lift. While the force and moment trends for both wings are similar, the rate of their change remains a function of their fabric stiffness'.

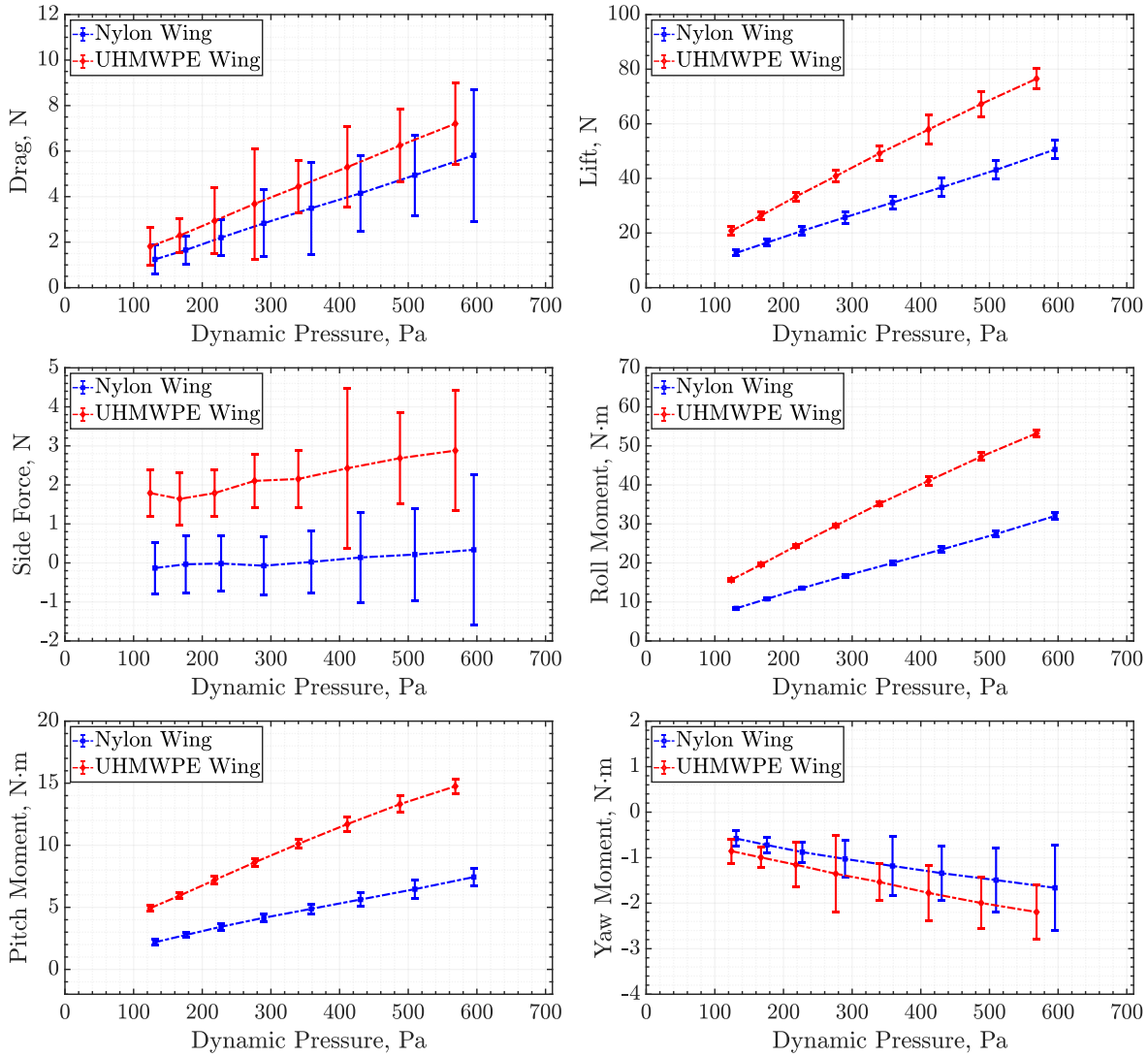

Fig. 18 Comparison of Forces and Moments between the NYL100LE and DYN100LE Configurations

Figure 19 compares the NYL100LETE and DYN100LETE cases. Like the previous comparison, the UHMWPE wing has greater lift and drag than the nylon wing. However, the nylon wing has a more non-linear relationship with dynamic pressure due to the wing being more flexible. The positive twist induced in the wing mid-section for both wings forms the basis for this non-linear increase in lift and moments. The NYL77LE and DYN77LE case comparison (see Fig. 20) yields a slightly different inference for the drag, potentially due to greater form drag. This could be due to greater out-of-plane displacements for the nylon wing. The differences seen in the lift and moments are much more significant (more than $\sim$ 100% at 27.5 m/s wind tunnel speed).

In addition to the force and moment comparisons so far, insight may also be gained by looking at the lift coefficient

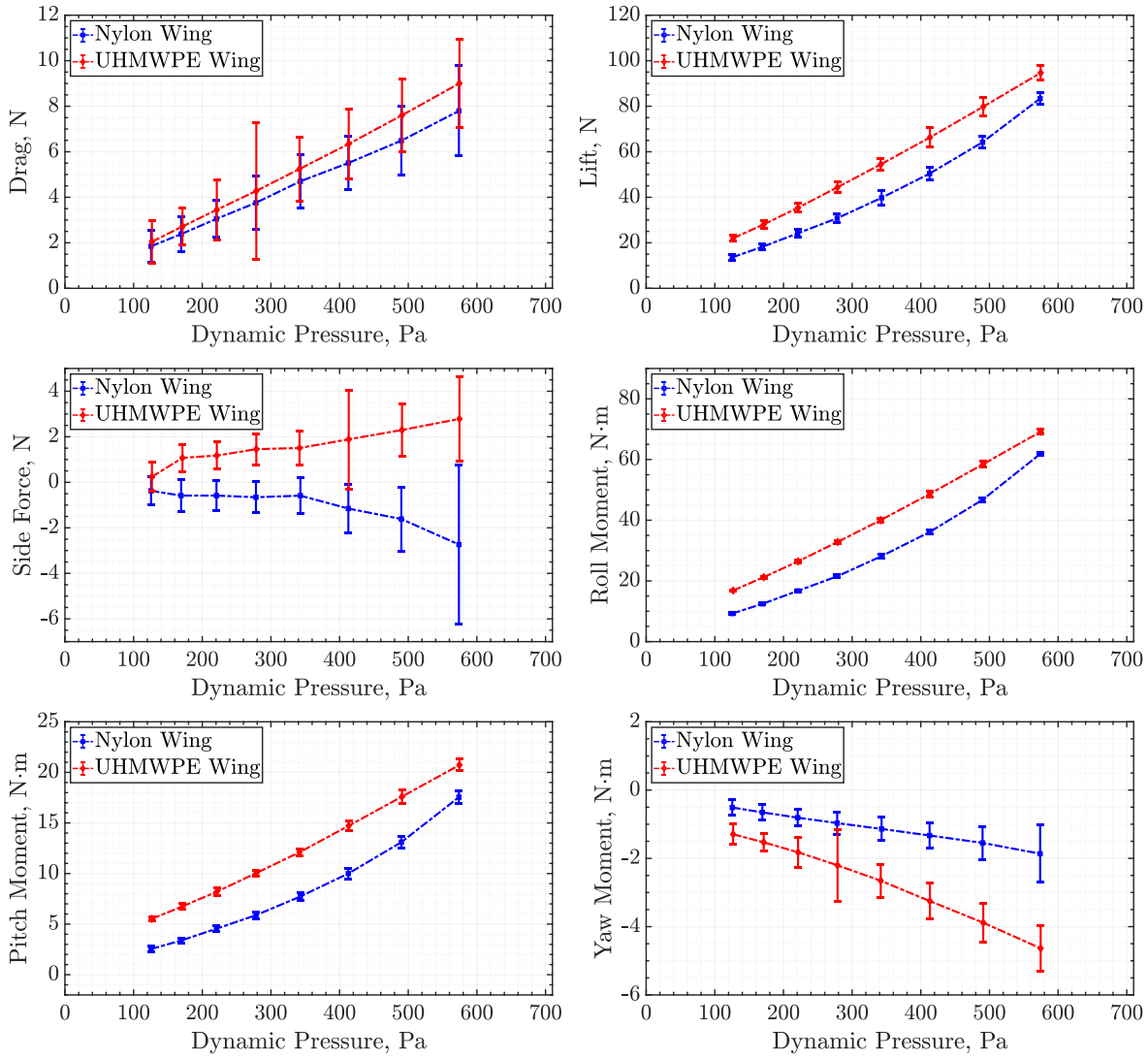

Fig. 19 Comparison of Forces and Moments between the NYL100LETE and DYN100LETE Configurations

as a function of dynamic pressure as seen in Fig. 21. The trends discussed earlier do hold for the lift coefficient albeit post some linearization due to division by the dynamic pressure. Interestingly, for the stiffer UHMWPE wing, the trends remain similar for all three cases at the lower dynamic pressure but as the dynamic pressure increases, the trends resemble those of the nylon wing. The lift coefficient for the UHMWPE wing is consistently greater than that of the nylon wing for all cases (as expected due to the right twist in the wing). These inferences illustrate an important outcome of this research. They highlight that the choice of fabric material plays a major role in determining the aerodynamic performance of such wings. These inferences, in conjunction with those from the previous sections, also illustrate the potential of passive aeroelastic tailoring of the wing design to obtain desirable aerodynamic behavior. This tailoring can be in the form of high-lift producing configurations at low wind speeds (as with the NYL100LETE/DYN100LETE cases) or passive load alleviation at high speeds (as seen in the NYL77LE/DYN77LE cases).

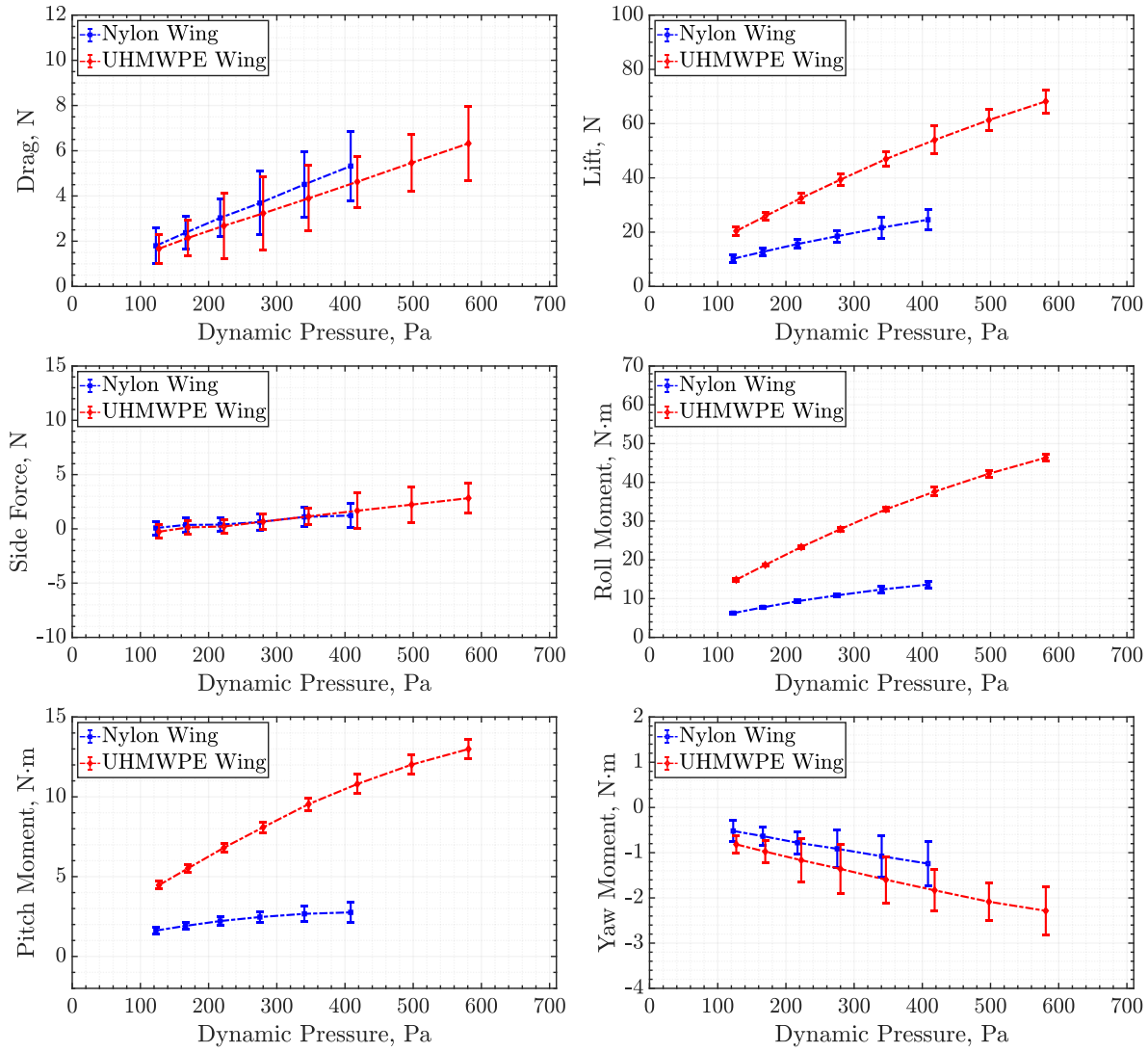

Fig. 20 Comparison of Forces and Moments between the NYL77LE and DYN77LE Configurations

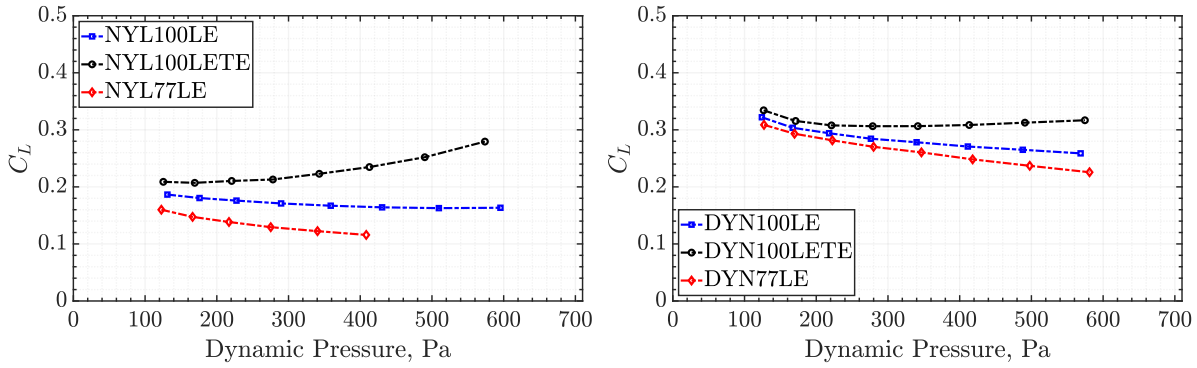

(a) **(b)**

Fig. 21 Lift Coefficient Comparisons for (a) the Nylon Wing and (b) the UHMWPE Wing

C. Wake Survey Results

Along with static aeroelastic and force and moment measurements, pressure measurements in the wing wake were also taken during this test. The purpose of these measurements was to provide some additional insight into the flow over the wings and serve as a set of validation data for comparison with high-fidelity computational fluid dynamics simulations. Section II.C details the setup and test structure for these pressure measurements. Figure 22 illustrates the wake total pressure coefficient for each of the three tether attachment cases in the nylon wing wake at the mid-height of the test section exit. This provides insight into the movement of the wake due to static aeroelastic displacements in the wing. The wake surveys (see Fig. 23), on the other hand, illustrate the various flow features in the wing wake.

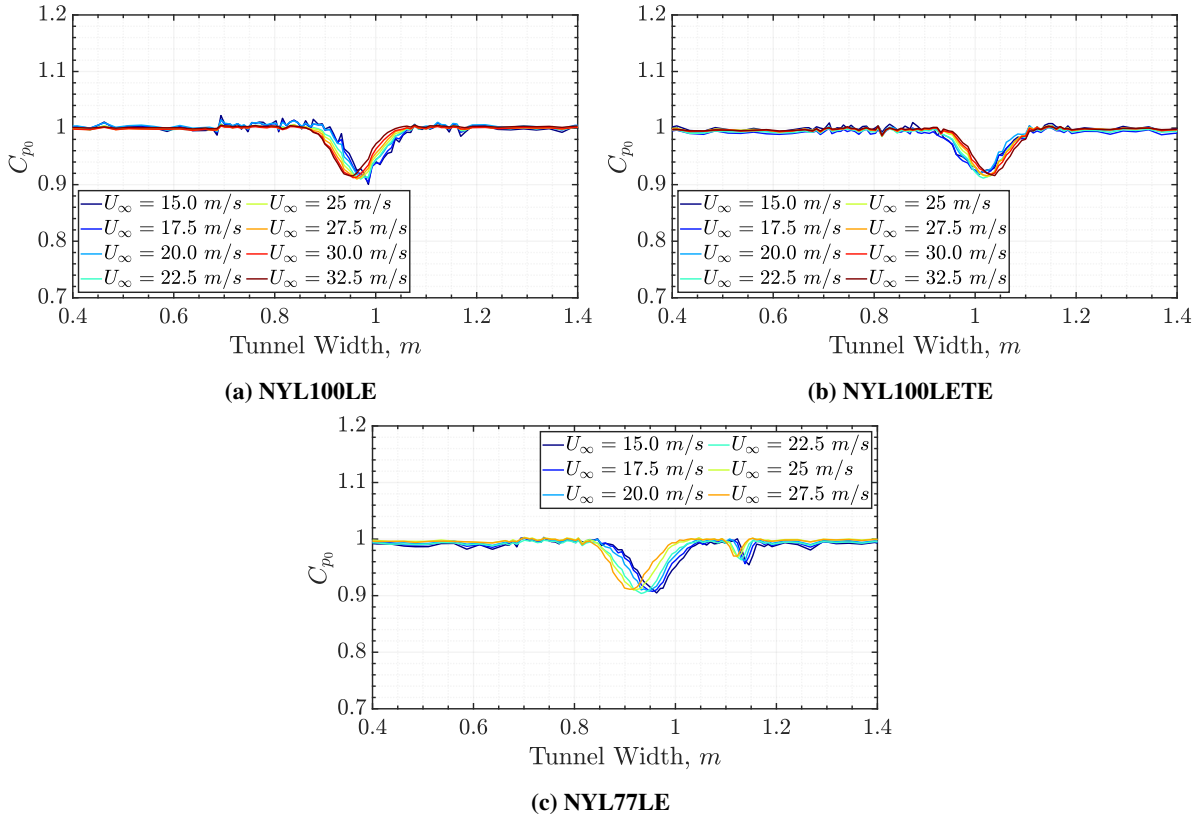

(a) NYL100LE

(b) NYL100LETE

(c) NYL77LE

Fig. 22 Wake C_{p_0} Variation with Wind Tunnel Speed at 3 ft. from Tunnel Floor for the Nylon Wing

During the speed runs for the NYL100LE case, the wake shifts towards the portside wall with an increase in wind tunnel speed as expected due to the variation in the static aeroelastic displacements and twist distributions. The NYL77LE case exhibits similar behavior regarding the trends in the wake movement, but the magnitude of the shift is greater due to its greater bending displacements. The wake of the tether is also visible in the wake profile as a drop in the total pressure coefficient. This indicates that the contribution of the tether drag to the total drag on the test article could be significant. For the NYL100LETE case, the wake shifts to the right (towards the starboard wall) with an increase in wind tunnel speed, as expected from the positive twist angle induced in the wings' mid-section.

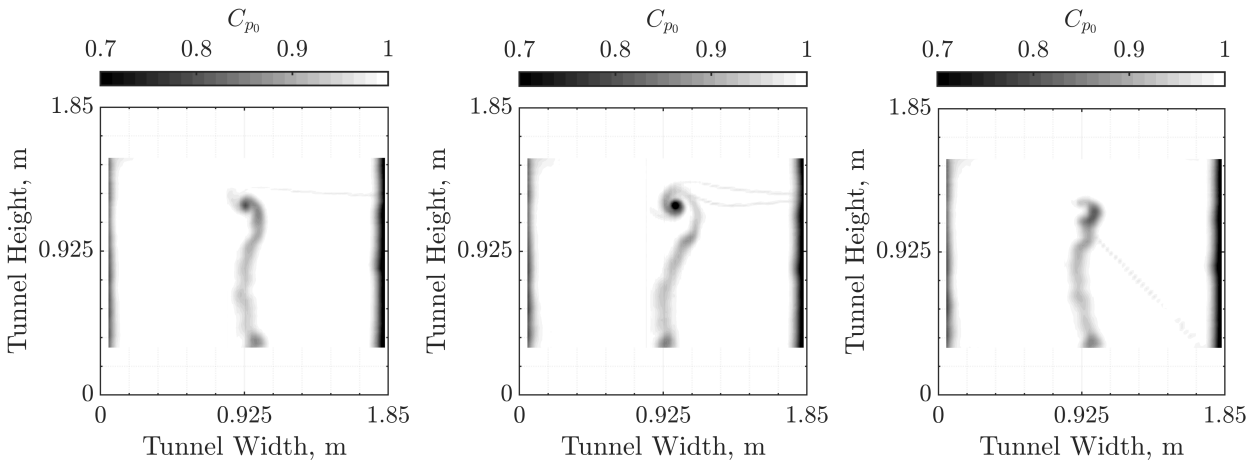

(a) NYL100LE **(b) NYL100LETE** **(c) NYL77LE**

Fig. 23 Experimental Wake C_{p_0} Contours for the Nylon Wing Configurations for $U_\infty = 27.5\ m/s$

The experimental traversing wake Pitot pressure coefficient contours for the Nylon wing are shown in Fig. 23. The Pitot pressure coefficient contours depict regions of flow where there is a Pitot pressure loss and hence, drag. This also indicates regions of flow where vortices are present. This is evident from the tip-vortex structures visible in contours. From these contours, one can also infer the variability in the strength of the tip vortex with changes in the tether configuration. For the NYL100LE and NYL100LETE configurations, a spiral-like wake vortex structure is seen, similar to those observed in rigid wings [49]. For the NYL77LE case, there seems to be some stretching of the tip vortex structure. Additional interesting features in the wake are also visible, such as the tether wake and the mount tip vortex from the mount-wing junction region.

Figure 24 illustrates the wake total pressure coefficient profiles for the three tether attachment configurations for the UHMWPE wing. Like the NYL100LE case, the DYN100LE case has the wake shift to the left (towards the port wall) with an increase in wind tunnel speed. Unlike the Nylon wing, the magnitude of the Pitot pressure coefficient loss in the wake and tip vortex increases with wind tunnel speed. The location of the wing wake is skewed more towards the starboard wall when compared to the Nylon wing. The DYN100LETE case follows a similar trend indicating that bending plays a greater role in the determination of the wake location for this case compared to the twist. The wake measurements at the lowest speed (15 m/s) seem to be distorted for this configuration. The DYN77LE case follows the same trend observed in the NYL77LE case. Figure 25 shows the experimental wake total pressure coefficient contours at 27.5 m/s for all three tether attachment cases for the UHMWPE wing. Unlike the nylon wing, waviness is observed in the wake's shape, likely due to the warpage in this wing. The magnitude of the Pitot pressure loss is greater for this wing than that of the nylon wing. This is a result of the UHMWPE wing generating much greater lift. Spiral structures from the wake and tip vortex interaction are also visible along with the wake of the tether. The wake profiles are similar for the three UHMWPE wing cases due to lower static aeroelastic displacements than the Nylon wing at 27.5 m/s.

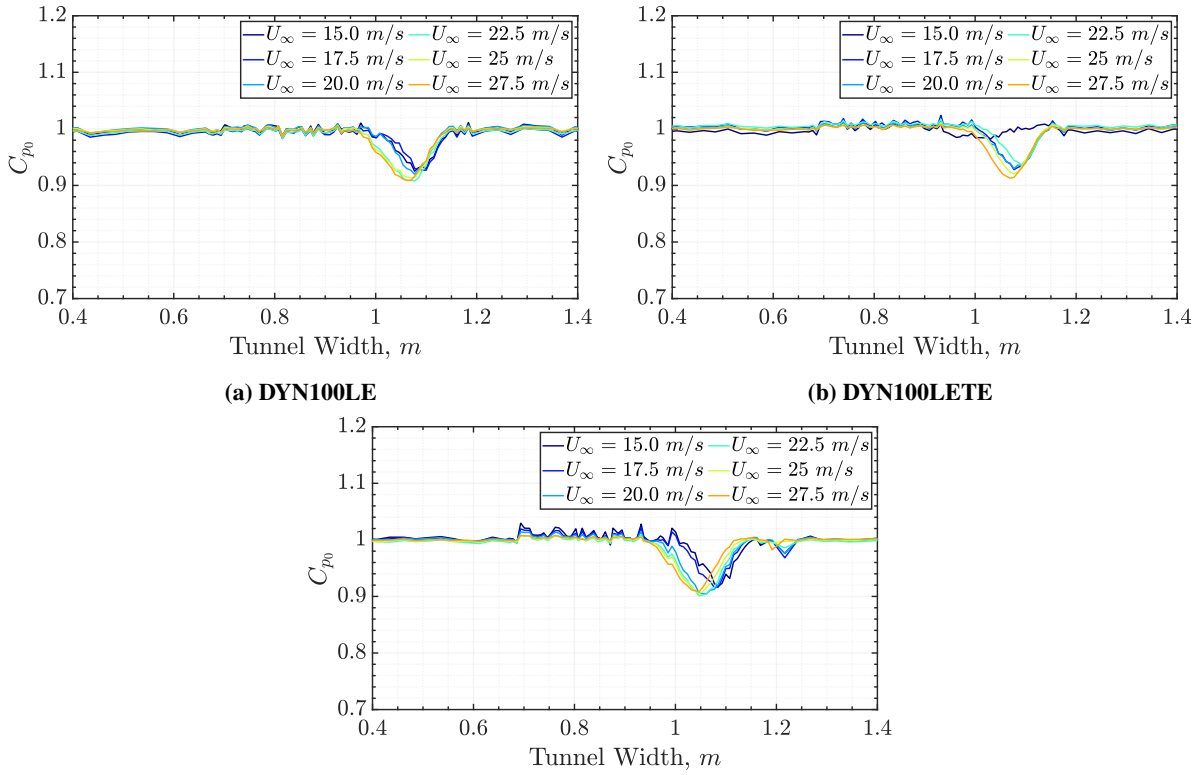

(a) DYN100LE **(b) DYN100LETE**

(c) DYN77LE

Fig. 24 Wake C_{p_0} Variation with Wind Tunnel Speed at 3 ft. from Tunnel Floor for the UHMWPE Wing

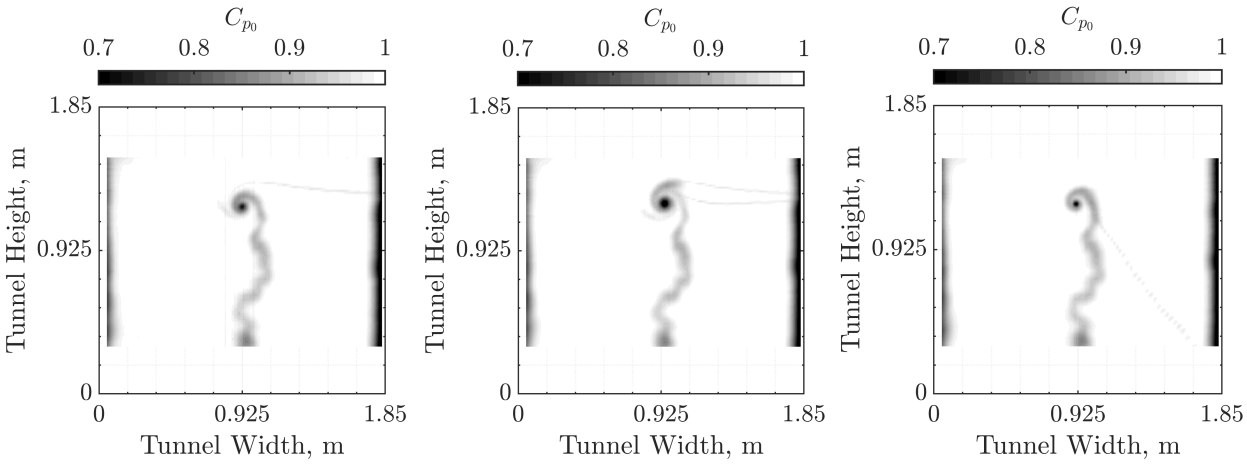

(a) DYN100LE **(b) DYN100LETE** **(c) DYN77LE**

Fig. 25 Experimental Wake C_{p_0} Contours for the UHMWPE Wing Configurations for $U_\infty = 27.5\ m/s$

IV. Conclusions and Future Work

This paper presents wind tunnel tests of two swept, tethered, flexible inflatable wings in the Virginia Tech Stability Wind Tunnel conducted over a speed range of 15.0 m/s to 32.5 m/s at a fixed angle of attack. One wing is constructed out of Nylon 200D fabric, while the other is made of UHMWPE fabric. Non-contact displacement field measurements

and forces and moments were recorded for three different tether attachment configurations for each wing. Wake surveys were also conducted at 27.5 m/s for all three tether attachment configurations for each wing to obtain the Pitot pressure coefficient in the wake of the wings, which reveals interesting flow features in the wing wake such as the tip vortex, the tether wake, and the vortex near the wing-mount junction. This experiment details an approach for experimental testing of such wings while providing a comprehensive dataset for aeroelastic model validation and high-fidelity CFD studies.

Key findings illustrate the effect that tether attachment location and orientation, along with the stiffness of the fabric material of the wings, have on the aerodynamic forces and moments generated by the wing. Furthermore, these findings also provide avenues for passive aeroelastic tailoring of the wing for generating higher lift at low speeds or passive load alleviation at higher speeds. Such aeroelastic tailoring can potentially result in significant weight savings for tethered kite-like systems by contributing to the reduction in complexity and energy requirements for the stability and control of a kite. As a consequence, future efforts will be directed toward passive or active aeroelastic tailoring that can be initiated by altering the tether locations and the number of tethers, as well as the use of smart materials and novel actuators for wing morphing. While these measurements are conducted for a wing in a cantilevered boundary condition, the inferences from this experiment can aid in designing similar airborne wind energy systems in a free-free configuration. An interesting area of study is potentially looking at hysteresis effects in the forces and moments on such wings arising out of unsteady aerodynamics or dynamic variations in the wing twist due to aeroelastic deformations. Future efforts can also be directed towards the design of larger-scale inflatable wings where the effect of viscous forces may be noticeably different than the smaller-scale prototypes studied so far. For the realizability of such airborne wind energy systems, efforts need also be directed towards studying tether drag reduction technologies and other system redundancies in the event of adverse environmental effects.

Data Availability

All the data presented in this article, along with the inflatable wing scanned geometries, have been made available in a public repository: `https://doi.org/10.5281/zenodo.11293910`.

Funding Sources

The authors would like to acknowledge the funding and resources from Toyota Research Institute North America (TRINA) towards the successful completion of this work.

Acknowledgments

The authors would like to acknowledge the invaluable contributions of Dr. Jitish Miglani and Dr. Wei Zhao from Virginia Tech in the test planning phase and during testing. Many thanks are due Dr. Shardul Panwar, Azwan Aris, and Dr. Taewoo Nam of TRINA for their contributions to the test article design, construction, structural testing, and test

planning. Thanks are also due Prof. Aurelian Borgoltz, William Oetjens, and the Virginia Tech AOE machine shop staff.

References

[1] Hobbs, S., "Kite measurements in the boundary layer," *Wind Engineering*, 1989, pp. 50–60. URL https://www.jstor.org/stable/43749367.

[2] Loyd, M. L., "Crosswind kite power," *Journal of Energy*, Vol. 4, No. 3, 1980, pp. 106–111. https://doi.org/10.2514/3.48021.

[3] Ahrens, U., Diehl, M., and Schmehl, R., *Airborne Wind Energy*, Springer Science & Business Media, 2013. https://doi.org/10.1007/978-3-642-39965-7.

[4] Cherubini, A., Papini, A., Vertechy, R., and Fontana, M., "Airborne Wind Energy Systems: A review of the technologies," *Renewable and Sustainable Energy Reviews*, Vol. 51, 2015, pp. 1461–1476. https://doi.org/10.1016/j.rser.2015.07.053.

[5] Fagiano, L., and Milanese, M., "Airborne wind energy: an overview," *2012 American Control Conference (ACC)*, IEEE, 2012, pp. 3132–3143. https://doi.org/10.1109/ACC.2012.6314801.

[6] Schmehl, R., *Airborne wind energy: advances in technology development and research*, Springer, 2018. https://doi.org/10.1007/978-981-10-1947-0.

[7] Itakura, E., "Save from Future Japan Social Crises! 'Mothership' Project," *Airborne Wind Energy Conference (AWEC)*, Glasgow, UK, 15-16 October 2019. URL http://resolver.tudelft.nl/uuid:64fc750b-5d1b-4f83-873e-f308109a88b3, aWEC No. 65.

[8] Nam, T., Vahid, O., Gupta, R., and Kapania, R. K., "High Altitude Airborne Wind Energy," *AIAA SciTech 2021 Forum*, 2021, p. 1815. https://doi.org/10.2514/6.2021-1815.

[9] Gupta, R., Zhu, Y., and Nam, T., "Flight Dynamics, Control Law Design, and Flight Tests of Kite," *AIAA SciTech 2021 Forum*, 2021, p. 2462. https://doi.org/10.2514/6.2021-2462.

[10] Gupta, R., Zhu, Y., Nam, T., Tsukada, T., Fukagawa, T., and Itakura, E., "Crosswind Flight Dynamics Modeling of Tethered Kite," *AIAA SciTech 2022 Forum*, 2022. https://doi.org/10.2514/6.2022-0136.

[11] Zhu, Y., Gupta, R., Aris, A., and Nam, T., "Development and Flight Testing of the Flight Control System for a Tethered Wing," *AIAA SciTech 2022 Forum*, 2022. https://doi.org/10.2514/6.2022-2049.

[12] Rogallo, F. M., "NASA research on flexible wings," Tech. rep., 1967. URL https://ntrs.nasa.gov/citations/19680015821.

[13] Benedetti, D. M., and Veras, C. A. G., "Wind-Tunnel Measurement of Differential Pressure on the Surface of a Dynamically Inflatable Wing Cell," *Aerospace*, Vol. 8, No. 2, 2021, p. 34. https://doi.org/10.3390/aerospace8020034.

[14] Belloc, H., "Wind tunnel investigation of a rigid paraglider reference wing," *Journal of Aircraft*, Vol. 52, No. 2, 2015, pp. 703–708. https://doi.org/10.2514/1.C032513.

[15] Desabrais, K. J., Bergeron, K., Nyren, D., and Johari, H., "Aerodynamic Investigations of a Ram-Air Parachute Canopy and an Airdrop System," *23rd AIAA Aerodynamic Decelerator Systems Technology Conference*, 2015, p. 2145. https://doi.org/10.2514/6.2015-2145.

[16] Okda, S., Elbanhawy, A., Chernoray, V., Akl, W., and Elsabbagh, A., "Testing of the Aerodynamic Characteristics of an Inflatable Airfoil Section," *Journal of Aerospace Engineering*, Vol. 33, No. 5, 2020, p. 04020061. https://doi.org/10.1061/(ASCE)AS.1943-5525.0001187.

[17] Simpson, A., Smith, S., and Jacob, J., "Aeroelastic Behavior of Inflatable Wings: Wind Tunnel and Flight Testing," *45th AIAA Aerospace Sciences Meeting and Exhibit*, 2007, p. 1069. https://doi.org/10.2514/6.2007-1069.

[18] Cocke, B. W., *Wind-tunnel Investigation of the Aerodynamic and Structural Deflection Characteristics of the Goodyear Inflatoplane*, Vol. 23, National Advisory Committee for Aeronautics, 1958. URL https://ntrs.nasa.gov/citations/19930090147.

[19] Taylor, M., "Flying machine," , Apr. 25 1933. US Patent 1,905,298.

[20] Brown, G., Haggard, R., and Norton, B., "Inflatable structures for deployable wings," *16th AIAA Aerodynamic Decelerator Systems Technology Conference and Seminar*, 2001, p. 2068. https://doi.org/10.2514/6.2001-2068.

[21] Murray, J., Pahle, J., Thornton, S., Vogus, S., Frackowiak, T., Mello, J., and Norton, B., "Ground and flight evaluation of a small-scale inflatable-winged aircraft," *40th AIAA Aerospace Sciences Meeting & Exhibit*, 2002. https://doi.org/10.2514/6.2002-820.

[22] Norris, R., and Pulliam, W., "Historical Perspective On Inflatable Wing Structures," *50th AIAA/ASME/ASCE/AHS/ASC Structures, Structural Dynamics, and Materials Conference 17th AIAA/ASME/AHS Adaptive Structures Conference 11th AIAA No*, 2009, p. 2145. https://doi.org/10.2514/6.2009-2145.

[23] Cadogan, D., Graham, W., and Smith, T., "Inflatable and rigidizable wings for unmanned aerial vehicles," *2nd AIAA" Unmanned Unlimited" Conf. and Workshop & Exhibit*, 2003, p. 6630. https://doi.org/10.2514/6.2003-6630.

[24] Simpson, A., Usui, M., Smith, S., and Jacob, J., "Aeromechanics of inflatable airfoils," *34th AIAA Fluid Dynamics Conference and Exhibit*, 2004, p. 2233. https://doi.org/10.2514/6.2004-2233.

[25] Jacob, J., and Smith, S., "Design of HALE aircraft using inflatable wings," *46th AIAA Aerospace Sciences Meeting and Exhibit*, 2008, p. 167. https://doi.org/10.2514/6.2008-167.

[26] Cadogan, D., Smith, T., Lee, R., Scarborough, S., and Graziosi, D., "Inflatable and Rigidizable Wing Components for Unmanned Aerial Vehicles," *44th AIAA/ASME/ASCE/AHS/ASC Structures, Structural Dynamics, and Materials Conference*, 2003. https://doi.org/10.2514/6.2003-1801.

[27] Takahashi, D., and Lebeau, R., "Computational Investigation of Flow over Inflatable Airfoils at Multiple Reynolds Numbers," *49th AIAA Aerospace Sciences Meeting including the New Horizons Forum and Aerospace Exposition*, 2011. https://doi.org/10.2514/6.2011-377.

[28] Ghobadi, K., Lebeau, R., and Hauser, T., "Computational Testing of Inflatable Airfoils for Improved Design," *50th AIAA Aerospace Sciences Meeting including the New Horizons Forum and Aerospace Exposition*, 2012. https://doi.org/10.2514/6.2012-1213.

[29] Ghobadi, K., Pifer, E., Lebeau, R., Bramesfeld, G., and Mcquilling, M., "A Computational and Experimental Investigation of Flow Over an Inflatable Wing," *30th AIAA Applied Aerodynamics Conference*, 2012. https://doi.org/10.2514/6.2012-2899.

[30] Santhanakrishnan, A., and Jacob, J., "Effect of Regular Surface Perturbations on Flow Over an Airfoil," *35th AIAA Fluid Dynamics Conference and Exhibit*, 2005. https://doi.org/10.2514/6.2005-5145.

[31] Lebeau, R., Reasor, D., and Jacob, J., "Numerical Study of Bumpy Airfoil Flow Control for Low Reynolds Numbers," *37th AIAA Fluid Dynamics Conference and Exhibit*, 2007. https://doi.org/10.2514/6.2007-4100.

[32] Gupta, R., Panwar, S., Nam, T., Miglani, J., Desai, S., and Kapania, R. K., "Aeroelastic Analysis and Wind Tunnel Flutter Testing of Inflatable Tethered Wing," *AIAA SciTech 2024 Forum*, 2024, p. 2099. https://doi.org/10.2514/6.2024-2099.

[33] Panwar, S., Gupta, R., Aris, A., Nam, T., Miglani, J., Zhao, W., and Kapania, R., "3-D Photogrammetric Modal Testing and Data Analysis of a Cantilever Inflatable Wing," *AIAA SciTech 2022 Forum*, 2022. https://doi.org/10.2514/6.2022-1513.

[34] Miglani, J., Zhao, W., Kapania, R. K., Panwar, S. S., Gupta, R., and Aris, A., "Theoretical and Experimental Analyses of Inflatable Structures," *AIAA SciTech 2023 Forum*, 2023, p. 0385. https://doi.org/https://doi.org/10.2514/6.2023-0385.

[35] "Virginia Tech Stability Wind Tunnel," , 2022. URL https://www.aoe.vt.edu/research/facilities/stabilitytunnel.html.

[36] Vishwanathan, V., Szoke, M., Duetsch-Patel, J. E., Gargiulo, A., Fritsch, D. J., Borgoltz, A., Roy, C. J., Lowe, K. T., and Devenport, W. J., "Aerodynamic design and validation of a contraction profile for flow field improvement and uncertainty quantification in a subsonic wind tunnel," *AIAA SciTech 2020 Forum*, 2020, p. 2211. https://doi.org/10.2514/6.2020-2211.

[37] Duetsch-Patel, J. E., Vishwanathan, V., Minionis, J. B., Totten, E., Gargiulo, A., Fritsch, D. J., Szoke, M., Borgoltz, A., Roy, C. J., Lowe, K. T., et al., "Aerodynamic Design and Assessment of Modular Test Section Walls for CFD Validation in Hybrid Anechoic Wind Tunnels," *AIAA SciTech 2020 Forum*, 2020, p. 2214. https://doi.org/10.2514/6.2020-2214.

[38] "Dyneema® Fabric," , 2022. URL https://www.dsm.com/dyneema/en_GB/home.html.

[39] Abbott, I. H., and Von Doenhoff, A. E., *Theory of wing sections: including a summary of airfoil data*, Courier Corporation, 2012.

[40] Zhao, W., Desai, S., Miglani, J., Kapania, R. K., Schetz, J. A., Aris, A., and Panwar, S. S., "Structural and Aeroelastic Design, Analysis, and Experiments of Inflatable Airborne Wings," *AIAA SciTech 2021 Forum*, 2021, p. 1817. https://doi.org/10.2514/6.2021-1817.

[41] Desai, S. P., Schetz, J. A., Aris, A., Panwar, S. S., and Gupta, R., "Wind Tunnel Experiments and Numerical Investigation of the Aerodynamics of an Inflated Wing," *AIAA SciTech 2022 Forum*, 2022, p. 0903. https://doi.org/10.2514/6.2022-0903.

[42] Dong, Y., and Pan, B., "In-situ 3D shape and recession measurements of ablative materials in an arc-heated wind tunnel by UV stereo-digital image correlation," *Optics and Lasers in Engineering*, Vol. 116, 2019, pp. 75–81. https://doi.org/10.1016/j.optlaseng.2018.10.022.

[43] "GOM-Precise Industrial 3D Metrology," , 2021. URL https://www.gom.com/en/.

[44] Kuester, M. S., Borgoltz, A., and Devenport, W. J., "Pressure tap effects on the lift measurement of an airfoil section," *32nd AIAA Aerodynamic Measurement Technology and Ground Testing Conference*, 2016, p. 3654. https://doi.org/10.2514/6.2016-3654.

[45] Szoke, M., Vishwanathan, V., Loeschen, T., Gargiulo, A., Fritsch, D. J., Duetsch-Patel, J. E., Borgoltz, A., Roy, C. J., Lowe, K. T., and Devenport, W. J., "Developing a Numerical Model of the Virginia Tech Stability Wind Tunnel for Uncertainty Quantification Based On Real-World Geometry," *AIAA SciTech 2020 Forum*, 2020, p. 0343. https://doi.org/10.2514/6.2020-0343.

[46] "Next Generation Conceptual Aero Structural Sizing," , 2021. URL https://www.neocass.org/.

[47] Song, Y., Gandhi, U., and Aris, A., "A Baffled Inflatable Wing made from High Performance Textile Materials: Design, Analysis, and Experiments," *AIAA SciTech 2021 Forum*, 2021, p. 0430. https://doi.org/10.2514/6.2021-0430.

[48] "Autodesk Meshmixer," , 2022. URL https://www.meshmixer.com/.

[49] Devenport, W. J., Rife, M. C., Liapis, S. I., and Follin, G. J., "The structure and development of a wing-tip vortex," *Journal of Fluid Mechanics*, Vol. 312, 1996, pp. 67–106. https://doi.org/10.1017/S0022112096001929.